ORIGINAL PAPER

Emiliano Matta● · Rita Greco

Modeling and design of tuned mass dampers using sliding variable friction pendulum bearings

Abstract An effective vibration control device, the pendulum tuned mass damper (P-TMD), can be easily realized as a mass supported on rolling or sliding pendulum bearings. While the bearings' concavity provides the desired gravitational restoring force, the necessary dissipative force can be obtained either from additional dampers installed in parallel with the bearings or from the same friction resistance developing within each bearing between the roller/slider and the rolling/sliding surface. The latter solution may prove cheaper and more compact but implies that the P-TMD effectiveness will be amplitude dependent if the friction coefficient is kept uniform along the rolling/sliding surface, as in conventional friction bearings. In this case, the friction P-TMD will be as efficient as a viscous P-TMD only at a given vibration level, with large performance reductions at other levels. To avoid this inconvenience, this paper proposes a new type of sliding variable friction pendulum (VFP) TMD, called the VFP-TMD, in which the sliding surface is divided into two concentric regions: a circular inner region, having the lowest possible friction coefficient and the same dimensions of the slider, and an annular outer region, having a friction coefficient set to an optimal value. A similar arrangement has been recently proposed to realize adaptive seismic isolation devices, but no specific application to TMDs is reported. To assess the VFP-TMD performance, first its analytical model is derived, rigorously accounting for geometric nonlinearities as well as for the variable (in time and space) pressure distribution along the contact area, and then, an optimal design methodology is presented. Finally, numerical simulations show the influence of the main design parameters on the device behavior and demonstrate that the VFP-TMD can achieve nearly the same effectiveness of viscous P-TMDs, while considerably outperforming conventional uniform-friction P-TMDs. The proposed analytical model can be used to enhance or validate existing models of VFP isolators that assume a constant and uniform contact pressure distribution.

1 Introduction

Tuned mass dampers (TMDs) are well-known passive control devices, extensively studied and widely applied for the vibration mitigation of low-damped structures under natural and anthropic loads [1–6]. A TMD is essentially a single-degree-of-freedom (SDOF) oscillator attached to the main structure, dynamically interacting with a selected target structural mode by frequency tuning and damping optimization, and consequently absorbing and dissipating part of its vibrational energy [7]. To control horizontal vibrations, pendulum TMDs (P-TMDs) are commonly employed, using gravity to produce the required restoring force, and consisting of

E. Matta (✉)
Department of Architecture and Design, Politecnico di Torino, Viale Mattioli 39, 10125 Turin, Italy
E-mail: emiliano.matta@polito.it

R. Greco
Department of Civil, Environmental, Territory, Building and Chemical Engineering, Politecnico di Bari, Via Orabona 4, 70126 Bari, Italy

damped masses constrained to move along curved profiles or surfaces, whose curvature determines the P-TMD natural frequency. While hanging-type P-TMDs are suspended by ropes or bars [8], supported-type P-TMDs roll or slide on concave tracks or bearings [9]. Increasing interest for supported P-TMDs has been recently observed, because of their greater compactness, durability, and versatility in shape. This has resulted in the availability of various supported P-TMDs configurations, including rolling and sliding P-TMDs [10], ball-type P-TMDs [11], unbalanced rolling P-TMDs [12], and track nonlinear energy sinks [13]. Each configuration can be realized as a unidirectional or a bidirectional arrangement, in this latter case recurring either to a pair of orthogonal tracks mounted in series, or to one three-dimensional (3D) optimal surface, non-axial–symmetrical when the two principal frequencies of the main structure are different [14].

Whatever the configuration, two main solutions exist to provide a supported P-TMD with the required energy dissipation capability. The first consists in connecting its mass to the structure by an additional dissipative link, e.g., a linear viscous damper [14]. The second consists in exploiting the rolling or sliding friction resistance developing along the pendulum surface during P-TMD motion [15]. Avoiding the additional damping devices, this second solution is simpler, more compact, and potentially cheaper than the first one, and always adopted in ball-type P-TMDs [16–18]. However, as long as the friction coefficient is uniform along the surface, the friction force is virtually constant [19], which makes the P-TMD equivalent damping ratio inversely proportional to the P-TMD displacement amplitude, and the P-TMD effectiveness amplitude dependent [15,20]. To avoid this inconvenience, inspired by the homogeneous friction concept proposed by Inaudi and Kelly [21] and developed by Almazan et al. [8], Matta [22] proposed a new type of supported P-TMD, characterized by a friction coefficient that varies along the pendulum surface proportionally to the modulus of the surface gradient. In the first-order approximation, such friction model is nonlinear but homogeneous: the friction force increases proportionally to the radial displacement, and the P-TMD effectiveness results amplitude independent. By an appropriate choice of the proportionality coefficient, the optimal friction pattern is determined, and the same performance of an optimal viscous P-TMD is obtained, for any vibration level. Theoretically applicable to both rolling and sliding P-TMDs, the concept has been experimentally validated on small-scale prototypes of rolling P-TMDs [22] and ball-type P-TMDs [23], where the continuous optimal friction pattern is approximated by coating the rolling surface with a series of concentric rubber layers of increasingly larger friction properties.

Focusing on spherical sliding P-TMDs, this paper proposes a new type of variable friction pendulum (VFP) TMD, called the VFP-TMD, in which each sliding surface is divided into two concentric regions: an inner circular region, having the lowest possible friction coefficient and the same dimensions of the slider, and an outer annular region, having a friction coefficient set to an optimal value (Fig. 1). In this way, as the slider
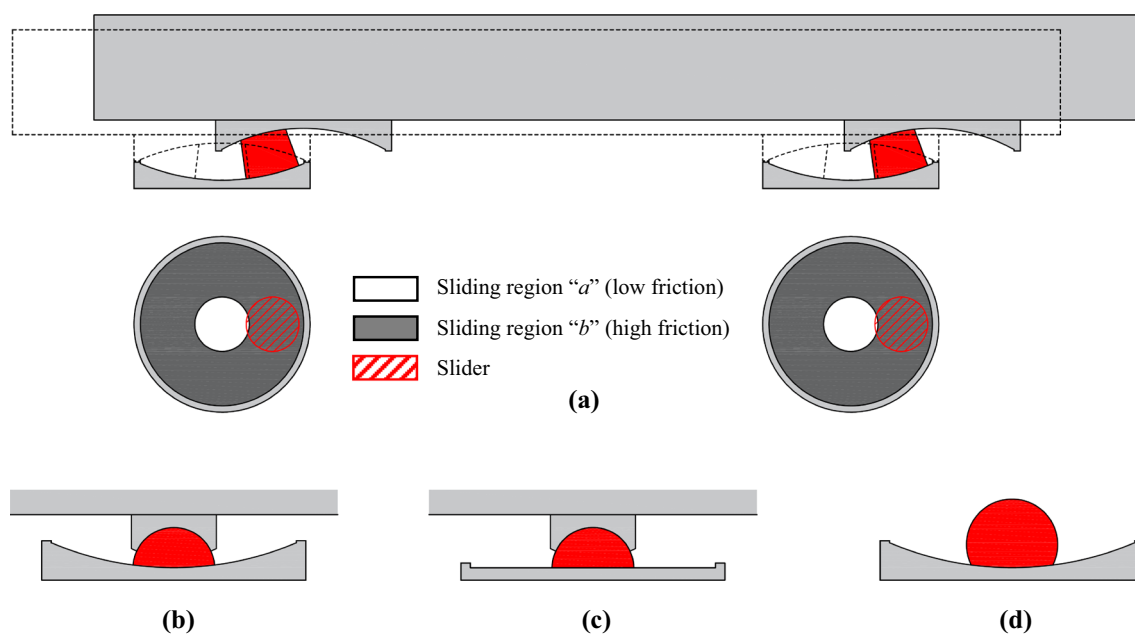
Fig. 1 Some possible arrangements of a VFP-TMD: **a** the absorber on two double pendulum bearings (lateral and planar views); **b** single pendulum bearing; **c** flat bearing; **d** rocking pendulum TMD
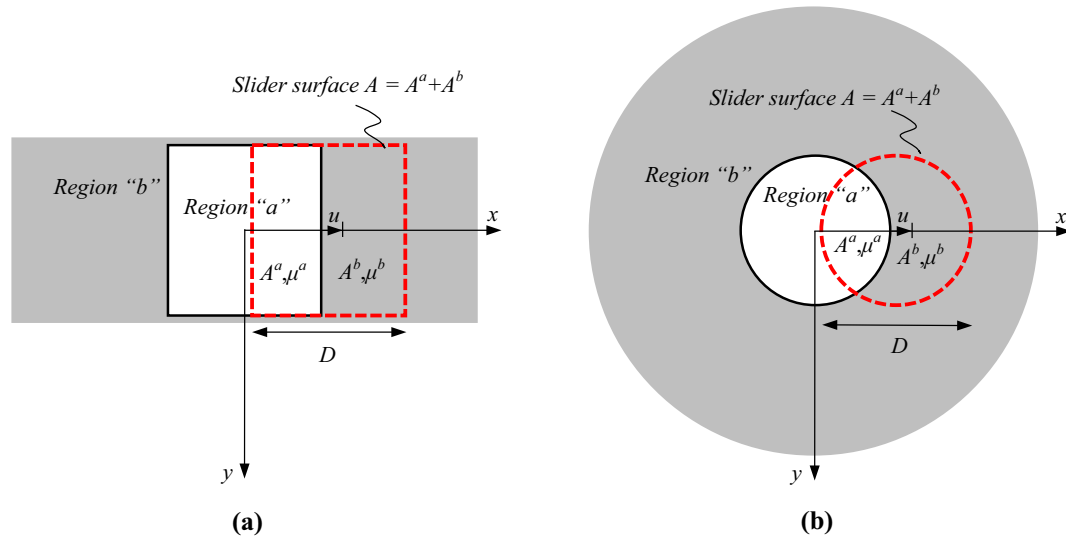
Fig. 2 Planar view of a flat slider moving along x on a two-region flat sliding surface, the inner region having the same dimensions of the slider: **a** rectangular slider; **b** circular slider. A^a and A^b are the contact areas between the slider and, respectively, the inner region "a" and the outer region "b," while μ^a and μ^b are their respective friction coefficients

moves across the two regions, the effective friction coefficient changes as a monotonic increasing function of its radial displacement. A similar arrangement has been recently adopted to realize "adaptive" seismic isolators, although several concentric regions are in that case generally admitted. VFP isolators have been postulated in [24], proposed in [25–27], and later analyzed by several authors (e.g., [28,29]). They are meant to outperform conventional friction pendulum bearings [30] by undergoing desired stiffness and damping modifications at specified displacement amplitudes, so that the isolation system can be optimized for multiple performance objectives [31]. With respect to multiple friction pendulums [32,33], VFP isolators can achieve this without increasing the number of sliding surfaces. Although a research program involving experimental activities is reportedly ongoing [28], no experimental results have been published to date. On the other hand, the literature reports extensive simulations of VFP isolators, showing them a viable alternative to traditional systems. These simulations are generally performed on simplified analytical models, neglecting second-order effects and assuming a uniform pressure on the contact area. To the authors' knowledge, no specific application of VFPs to TMDs is reported.

The VFP-TMD proposed in this paper consists of a mass (upper mass) supported on one or more VFP bearings. Figure 1a shows one possible arrangement, comprising two identical VFP bearings, each consisting of a double friction pendulum. According to this (planar) scheme, each bearing is made of two concave plates and a slider in between. For each VFP, the lower and upper sliding surfaces may differ from each other in shape and material properties. Figure 1b, c shows two alternative arrangements, in which the double pendulum is replaced with, respectively, a single pendulum bearing (Fig. 1b) and a flat bearing (Fig. 1c). In this latter case, horizontal springs should be added in parallel, not shown for brevity. A rocking pendulum arrangement is shown in Fig. 1d, in which the slider and the upper mass coincide and a single sliding surface exists. Clearly, arrangements 1b to 1d are special cases of the general arrangement 1a. Figure 1a also identifies the low-friction inner region "a" (white color), as large as the slider, and the high-friction region "b" (gray color), thick enough to contain the slider. The edge of the sliding surface is raised to prevent excessive strokes.

In the remaining of this paper, the working principles of the VFP-TMD are demonstrated, and its effectiveness is compared to that of existing P-TMD types. To this aim, first its fully nonlinear analytical model is derived, then an optimal design method is proposed, and finally, numerical simulations are performed.

2 Analytical modeling of a VFP-TMD

This Section derives the fully nonlinear model of a VFP-TMD, based on the double pendulum arrangement shown in Fig. 1a. The model is first obtained for the device alone and then augmented to include the main structure. For simplicity, the motion is supposed to occur in a vertical plane, and the model is planar.
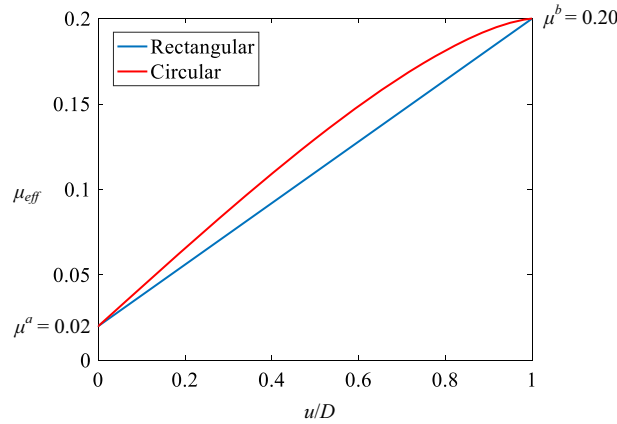
Fig. 3 Effective friction coefficient as a function of the normalized relative displacement, for the flat configurations depicted in Fig. 2, assuming $\mu^a = 0.02$ and $\mu^b = 0.20$

2.1 The variable friction concept

The variable friction concept is explained in Fig. 2, referring for simplicity to a single flat sliding surface. Denoting with x the axis of the relative sliding motion u, Fig. 2a, b, respectively, describes a rectangular slider of side length D (measured along x) and a circular slider of diameter D, sliding on a two-region flat surface, the inner region having the same shape and dimensions of the slider. In both figures, A^a and A^b are the contact areas between the slider and, respectively, the inner region "a" and the outer region "b," while μ^a and μ^b are their respective friction coefficients. Let $A = A^a + A^b$ be the area of the slider surface, $\sigma = \sigma(x, y)$ be the contact pressure distribution along A, and N be the normal contact force. Assuming a Coulomb friction model, the infinitesimal friction force dV exchanged through the generic infinitesimal area dA is

$$dV = \mu \sigma dA \tag{1}$$

where $\mu = \mu(x, y)$ is the friction coefficient distribution along A. Supposing the contact pressure uniform along A and therefore equal to $\sigma = N/A$ and denoting with V the tangential contact force, i.e., the friction force, the effective friction coefficient can be computed as the following function of u:

$$\mu_{\text{eff}} = \frac{V}{N} = \frac{1}{N} \int_A dV = \frac{1}{A} \int_A \mu(x, y) dA = \frac{1}{A}(\mu^a A^a + \mu^b A^b) = \mu^a + \left(\mu^b - \mu^a\right) \frac{A^b}{A} \tag{2}$$

where

$$\frac{A^b}{A} = \frac{|u|}{D} \leq 1 \tag{3}$$

for the rectangular case and

$$\frac{A^b}{A} = 1 - \frac{2}{\pi}\left(\alpha - \frac{|u|}{D} \sin \alpha\right) \leq 1 \tag{4}$$

for the circular case, with $\alpha = \arccos(|u|/D)$.

Equation (2) clearly shows that μ_{eff} is the average of the two friction coefficients, weighted by their respective contact areas. Equations (3) and (4) provide the relative weight of the outer region "b," which is a linear function of $|u|$ in the rectangular case and a nonlinear function of $|u|$ in the circular case.

Assuming, for example, $\mu^a = 0.02$ and $\mu^b = 0.20$, Fig. 3 shows μ_{eff} as a function of the slider normalized displacement, u/D. In the ideal case where the inner region was frictionless ($\mu^a = 0$), the rectangular configuration would ensure an exact proportionality between V and u, i.e., a homogeneous dissipative model, and the circular configuration a rough approximation of it, i.e., a nearly homogeneous dissipative model. On the other hand, the circular configuration has the advantage of being axial–symmetrical and therefore equally effective in every direction. Not shown in Fig. 3, if u exceeds D, then μ_{eff} will remain equal to μ^b in both cases, unless a third region is introduced with $\mu^c > \mu^b$, so that further increments are possible.
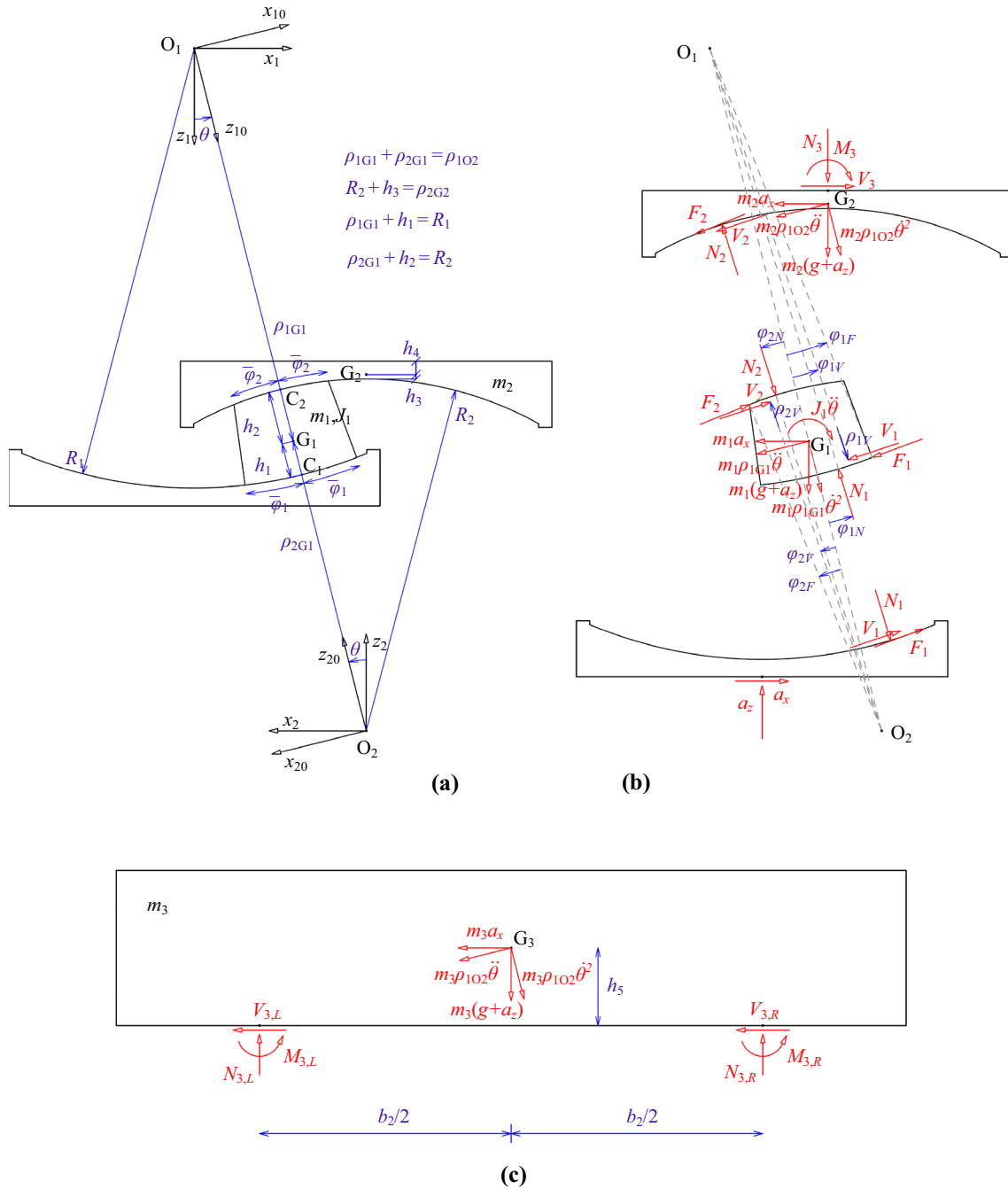
Fig. 4 Mechanical model of the VFP-TMD system. Geometry **(a)** and free-body diagram **(b)** of the individual VFP bearing. Geometry and free-body diagram of the TMD upper mass **(c)**. Blue color: dimensions; red color: forces (color figure online)

2.2 The general VFP-TMD model

2.2.1 Kinematic relations

The planar model of the double VFP-TMD shown in Fig. 1a is schematized in Fig. 4. Figure 4a, b depicts the geometry and the free-body diagram of each individual VFP bearing, while Fig. 4c shows the geometry and the free body diagram of the upper mass, supported on two identical VFP bearings. All bodies are assumed rigid. The motion is supposed to occur in the xz vertical plane, but the model accounts for the three dimensionalities
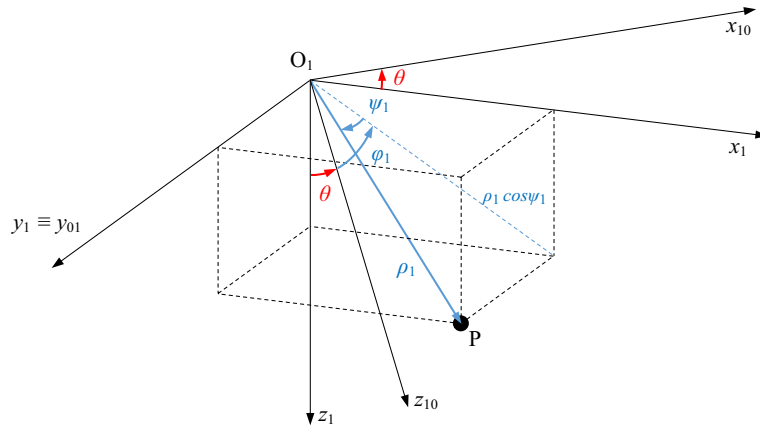
Fig. 5 Position of the generic point P of the slider according to the three local reference systems associated with the lower interface: $x_1 y_1 z_1$, $x_{10} y_{10} z_{10}$ and $\rho_1 \varphi_1 \psi_1$

of the spherical shape. Dimensions are in blue, and forces in red. For brevity, the subscripts "*L*" and "*R*," denoting in Fig. 4c the left and right bearings, are omitted in Fig. 4a, b, referring to the generic bearing, and will be avoided in the sequel unless necessary.

Each VFP bearing comprises a lower plate, integral with the main structure, an upper plate, integral with the upper mass, and a slider. The lower sliding and slider surfaces are spherical caps of radius R_1 and center O_1. The upper sliding and slider surfaces are spherical caps of radius R_2 and center O_2. C_1 and C_2 are the central points of the lower and upper slider surfaces. The slider has mass m_1, center of mass G_1, and central moment of inertia J_1. The upper plate has mass m_2 and center of mass G_2. The upper mass has mass m_3 and center of mass G_3. h_1 and h_2 are the distances of G_1 from C_1 and C_2; h_3 and h_4 are the distances of G_2 from the upper sliding surface and from the upper mass; h_5 is the height of G_3 above the upper plates; b is the relative distance between the two VFP bearings, symmetrical w.r.t. G_3.

For convenience, two local Cartesian coordinate systems are associated with each sliding interface. Referring to the lower interface, they are both centered in O_1: the system $x_1 y_1 z_1$ is integral with the lower plate (i.e., with the structure); the system $x_{10} y_{10} z_{10}$ is integral with the slider. Referring to the upper interface, they are both centered in O_2: the system $x_2 y_2 z_2$ is integral with the upper plate (i.e., with the TMD upper mass), and the system $x_{20} y_{20} z_{20}$ is integral with the slider.

The overall system has one degree of freedom, because the three rigid bodies are constrained by four double constraints (i.e., the sliding interfaces). No detachment is assumed possible at the sliding interfaces. Because the two VFP bearings are identical, the upper mass cannot rotate, and the coordinate systems $x_1 y_1 z_1$ and $x_2 y_2 z_2$ are parallel to each other and to the xyz system of the main structure, while the systems $x_{10} y_{10} z_{10}$ and $x_{20} y_{20} z_{20}$ are parallel to each other and rotated by a certain θ angle w.r.t. xyz. θ, being the counterclockwise rotation of the slider in the xz plane, is unique for the two VFP bearings and the only Lagrangian of the system.

Partially shown in Fig. 4 and better explained in Fig. 5, one further local coordinate system is associated with each sliding interface. Referring to the lower interface (the only one shown in Fig. 5, for brevity), this system, denoted as $\rho_1 \varphi_1 \psi_1$, is a polar system centered in O_1 and integral with the slider. According to this system, the position of any point P of the slider is expressed by ρ_1, i.e., the modulus of the vector $O_1 P$, by φ_1, i.e., the inclination of the plane containing $O_1 P$ and y_{10} w.r.t. the $y_{10} z_{10}$ plane, and by ψ_1, i.e., the inclination of $O_1 P$ w.r.t. the vertical plane $x_{10} z_{10}$. In this $\rho_1 \varphi_1 \psi_1$ system, all points on the slider surface have $\rho_1 = R_1$, and particularly C_1 has $\varphi_1 = \psi_1 = 0$, while the two points where the edge of the slider intersects the $x_1 z_1$ plane have $\psi_1 = 0$ and $\varphi_1 = \pm \bar{\varphi}_1$, where $\bar{\varphi}_1 > 0$ is the angular semi-width of the slider. In the same way, a polar system $\rho_2 \varphi_2 \psi_2$ is associated with the upper interface, centered in O_2 and integral with the slider.

The relations between the two Cartesian systems and the polar system are

$$x_i = \rho_i \cos \psi_i \sin(\varphi_i + \theta), \tag{5.1}$$

$$y_i = \rho_i \sin \psi_i, \tag{5.2}$$

$$z_i = \rho_i \cos \psi_i \cos(\varphi_i + \theta), \tag{5.3}$$

$$x_{i0} = x_i(\theta = 0) = \rho_i \cos \psi_i \sin \varphi_i, \tag{6.1}$$

$$y_{i0} = y_i(\theta = 0) = \rho_i \sin \psi_i = y_i, \tag{6.2}$$

$$z_{i0} = z_i(\theta = 0) = \rho_i \cos \psi_i \cos \varphi_i \tag{6.3}$$

where the subscript i stands for either 1 or 2, depending on which interface is referred to.

Equations (5.1), (5.2), (5.3), (6.1), (6.2), and (6.3) show that, during motion, any point of the slider undergoes a circular motion around each y_i axis, described by the radius $\rho_i \cos\psi_i$ and the angle $\varphi_i + \theta$. Considering in particular the point G_1 (characterized by $\rho_i = \rho_{iG1}$ and $\varphi_i = \psi_i = y_i = 0$), its motion w.r.t. O_i is given by $x_{iG1} = \rho_{iG1} \sin\theta$ and $z_{iG1} = \rho_{iG1} \cos\theta$. This implies that the motion of O_2 w.r.t. O_1 is given by $x_{1O2} = \rho_{1O2} \sin(\theta)$ and $z_{1O2} = \rho_{1O2} \cos\theta$, with $\rho_{1O2} = \rho_{1G1} + \rho_{2G1} = R_1 + R_2 - (h_1 + h_2)$, as evident in Fig. 4a. Because the upper mass translates like O_2, ρ_{1O2} represents the equivalent radius of the upper mass and indeed the equivalent radius of the entire TMD system if the slider mass is negligible.

2.2.2 Dynamic equations

Figure 4b and 4c shows the free-body diagrams of the VFP-TMD components. Denoting as a_x and a_z the horizontal and vertical components of the structural acceleration imparted to the lower plate, the actions on the various system components include weights, inertia forces and moments, contact forces, restrainer forces, and connection forces. In particular, the contact forces N_i and V_i are the resultants of, respectively, the pressures and the friction forces at the ith interface, while the restrainer force F_i is the force between the slider and the raised edge of the ith sliding surface. Because pressures are oriented toward O_i but generally not evenly distributed around C_i, N_i is directed toward O_i but inclined w.r.t. z_{i0} by an offset angle φ_{iN}. Because friction forces are tangential but generally not evenly distributed, and set at a variable distance $R_i \cos\psi_i \leq R_i$ from O_i, V_i is inclined by an angle φ_{iV} w.r.t. x_{i0} and set at a generic distance $\rho_{iV} \leq R_i$ from O_i. Because the restrainer force F_i arises at the contact point between the edge of the slider and the edge of the sliding surface, having coordinates $\rho_i = R_i, \varphi_i = \varphi_{iF} = \text{sgn}\,\theta\bar{\varphi}_i, \psi_i = 0$, it follows that F_i is tangentially applied at this point, i.e., inclined by an angle φ_{iF} w.r.t. x_{i0}, and set at a distance R_i from O_i. Finally, $N_{3,\text{L}}, V_{3,\text{L}}, M_{3,\text{L}}$ and $N_{3,\text{R}}, V_{3,\text{R}}, M_{3,\text{R}}$ are the connection forces and moments between the TMD upper mass and the upper plate of, respectively, the left and right bearings.

Based on the free-body diagrams of Fig. 4, the following 9 equations of motion are obtained:

$$m_1(g + a_z) \sin\theta + m_1 a_x \cos\theta + m_1 \rho_{1G1} \ddot{\theta} + N_1 \sin\varphi_{1N} + V_1 \cos\varphi_{1V},$$
$$+ F_1 \cos\bar{\varphi}_1 - N_2 \sin\varphi_{2N} - V_2 \cos\varphi_{2V} - F_2 \cos\bar{\varphi}_2 = 0, \tag{7.1}$$
$$m_1(g + a_z) \cos\theta - m_1 a_x \sin\theta + m_1 \rho_{1G1} \dot{\theta}^2 - N_1 \cos\varphi_{1N} + V_1 \sin\varphi_{1V}$$
$$+ \text{sgn}\,\theta \cdot F_1 \sin\bar{\varphi}_1 + N_2 \cos\varphi_{2N} - V_2 \sin\varphi_{2V} - \text{sgn}\,\theta \cdot F_2 \sin\bar{\varphi}_2 = 0, \tag{7.2}$$
$$J_1\ddot{\theta} - N_1\rho_{1G1} \sin\varphi_{1N} + V_1(\rho_{1V} - \rho_{1G1} \cos\varphi_{1V}) + F_1(R_1 - \rho_{1G1} \cos\bar{\varphi}_1)$$
$$- N_2\rho_{2G1} \sin\varphi_{2N} + V_2(\rho_{2V} - \rho_{2G1} \cos\varphi_{2V}) + F_2(R_2 - \rho_{2G1} \cos\bar{\varphi}_2) = 0, \tag{7.3}$$
$$[m_2(g + a_z) + N_3] \sin\theta + (m_2 a_x - V_3) \cos\theta + m_2\rho_{1O2} \ddot{\theta} + N_2 \sin\varphi_{2N}$$
$$+ V_2 \cos\varphi_{2V} + F_2 \cos\bar{\varphi}_2 = 0, \tag{7.4}$$
$$[m_2(g + a_z) + N_3] \cos\theta - (m_2 a_x - V_3) \sin\theta + m_2\rho_{1O2} \dot{\theta}^2 - N_2 \cos\varphi_{2N}$$
$$+ V_2 \sin\varphi_{2V} + \text{sgn}\,\theta \cdot F_2 \sin\bar{\varphi}_2 = 0, \tag{7.5}$$
$$M_3 + V_3 h_4 + N_2\rho_{2G2} \sin(\theta + \varphi_{2N}) + V_2[\rho_{2V} - \rho_{2G2} \cos(\theta + \varphi_{2V})]$$
$$+ F_2[R_2 - \rho_{2G2} \cos(\theta + \bar{\varphi}_2)] = 0, \tag{7.6}$$
$$V_{3,L} + V_{3,R} + m_3 a_x + m_3\rho_{1O2}(\ddot{\theta} \cos\theta - \dot{\theta}^2 \sin\theta) = 0, \tag{7.7}$$
$$N_{3,L} + N_{3,R} - m_3(g + a_z) - m_3\rho_{1O2}(\ddot{\theta} \sin\theta + \dot{\theta}^2 \cos\theta) = 0, \tag{7.8}$$
$$M_{3,L} + M_{3,R} - (N_{3,L} - N_{3,R})b/2 - (V_{3,L} + V_{3,R})h_5 = 0. \tag{7.9}$$

Equations (7.1)–(7.3) refer to the slider and are, respectively, written along x_{10}, along z_{10}, and around G_1. Equations (7.4)–(7.6) refer to the upper plate, respectively, along x_{20}, along z_{20}, and around G_2. Equations (7.7)–(7.9) refer to the upper mass, respectively, along x_2, along z_2, and around G_3. To completely describe the VFP-TMD system, Eqs. (7.1)–(7.6), referring to the individual VFP bearing, are to be written twice, i.e., once for the left bearing and once for the right, providing a total of 15 equations; 31 variables appear in these 15 equations. They include the Lagrangian θ (the only time-differentiated variable) plus 15 variables for each bearing, i.e., 6 contact/restrainer forces at each interface ($N_i, \varphi_{iN}, V_i, \varphi_{iV}, \rho_{iV}, F_i$) plus 3 connection forces and moments (N_3, V_3, M_3). The 16 missing equations required to solve the system are four constitutive
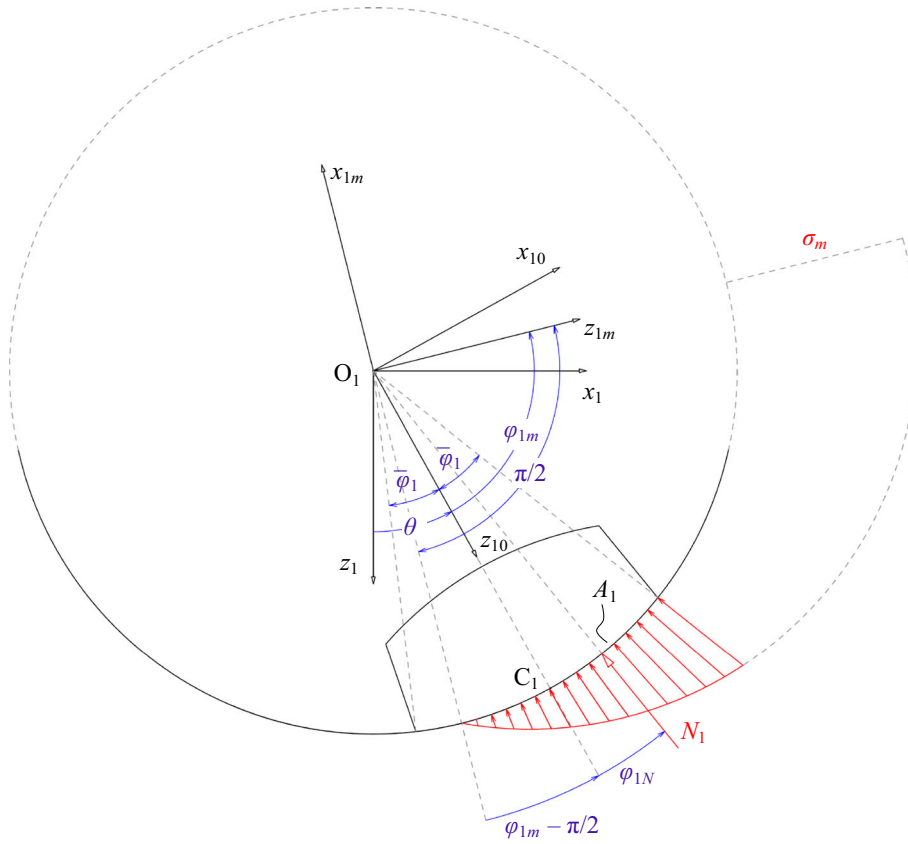
Fig. 6 Vertical section in the xz plane of motion of the pendulum TMD in its generic deformed position. Determination of the pressure distribution for an assigned $N_i - \varphi_{iN}$ pair

equations at each of the four interfaces, including: (i) three contact equations, providing V_i, φ_{iV} and ρ_{iV} as functions of N_i, φ_{iN}, θ and $\dot{\theta}$, and (ii) one restrainer equation, providing F_i as a function of θ and $\dot{\theta}$.

2.2.3 Constitutive equations

The three contact equations at each interface are obtained by the two-step procedure explained below.

As the first step, N_i and φ_{iN} are used to derive the distribution of pressures σ_i over the interface A_i. The problem is statically indeterminate, so the arbitrary assumption is made that

$$\sigma_i = \sigma_{im} \cos \psi_i \cos(\varphi_i - \varphi_{im}) \geq 0 \tag{8}$$

where σ_{im} is the maximum (real or virtual, depending if it falls within A_i or not) of the distribution, and φ_{im} is the offset angle of the plane containing σ_{im}. Figure 6, referring to the lower interface, exemplifies Eq. (8) when σ_{im} is virtual ($|\varphi_{im}| > \bar{\varphi}_i$) and the neutral axis (located at $\varphi_i = \varphi_{im} - \text{sgn}(\varphi_{im}) \cdot \pi/2$) intersects the interface A_i. Denoting with $x_{im} y_{im} z_{im}$ the local reference system obtained rotating $x_{i0} y_{i0} z_{i0}$ around y_{i0} by the angle φ_{im}, Eq. (8) states that σ_i is proportional to the distance from the $x_{im} y_{im}$ plane according to $\sigma_i = \sigma_{im} \cdot z_{im}/R_i$ and becomes null in the half-space where $z_{im} < 0$, as negative pressures are impossible. If the spherical surface tends to become flat (i.e., $\bar{\varphi}_i$, φ_i, and ψ_i tend to 0), Eq. (8) converges to $\sigma_i = \sigma_{im}(\cos \varphi_{im} + \varphi_i \sin \varphi_{im}) \geq 0$, corresponding to the Navier–Bernoulli planar beam section theory.

According to Eq. (8), the pressure distribution depends entirely on σ_{im} and φ_{im}, which on their turn can be determined by expressing the contact force N_i as the resultant of σ_i over A_i. Written along z_{i0} and around C_i, this equivalence, respectively, provides
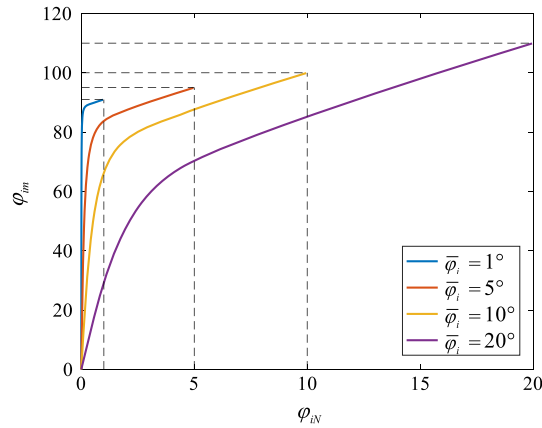
Fig. 7 Dependence of φ_{im} on φ_{iN} obtained by inverting Eq. (16), for 4 different values of $\bar{\varphi}_i$. Functions are plotted only for $\varphi_{iN} \geq 0$ because they are symmetrical with respect to $\varphi_{\mathrm{im}} = \varphi_{iN} = 0$

$$N_i \cos \varphi_{iN} = \int_{A_i} \sigma_i dA_i \cos \psi_i \cos \varphi_i$$

$$= \sigma_{\mathrm{im}} \int_{A_{ci}} \cos(\varphi_i - \varphi_{\mathrm{im}}) dA_i \cos^2 \psi_i \cos \varphi_i = \sigma_{\mathrm{im}} R_i^2 B_1(\bar{\varphi}_i, \varphi_{\mathrm{im}}) \qquad (9)$$

and

$$N_i \sin \varphi_{iN} R_i = \int_{A_i} \sigma_i dA_i \cos \psi_i R_i \sin \varphi_i$$

$$= \sigma_{\mathrm{im}} R_i \int_{A_{ci}} \cos(\varphi_i - \varphi_{\mathrm{im}}) dA_i \cos^2 \psi_i \sin \varphi_i = \sigma_{\mathrm{im}} R_i^3 B_2(\bar{\varphi}_i, \varphi_{\mathrm{im}}) \qquad (10)$$

where A_{ci} is the compressed part of A_i and functions B_1 and B_2 are detailed in Appendix A.

Dividing Eq. (10) by Eq. (9), the following relation is finally obtained:

$$\tan \varphi_{iN} = \frac{B_2(\bar{\varphi}_i, \varphi_{\mathrm{im}})}{B_1(\bar{\varphi}_i, \varphi_{\mathrm{im}})} = B_3(\bar{\varphi}_i, \varphi_{\mathrm{im}}). \qquad (11)$$

Remarkably, B_1, B_2 and therefore B_3 are functions of only $\bar{\varphi}_i$ and φ_{im}. Because $\bar{\varphi}_i$ is a constant parameter depending only on the slider's shape and B_3 is an odd monotonically increasing function of φ_{im}, then Eq. (11) univocally relates φ_{im} with φ_{iN}. Once φ_{im} is derived from φ_{iN} by inverting Eq. (11), σ_{im} is subsequently obtained from Eq. (9) as $\sigma_{\mathrm{im}} = N_i \cos \varphi_{iN}/[R_i^2 B_1(\bar{\varphi}_i, \varphi_{\mathrm{im}})]$.

So, the pressure distribution along each interface can be determined at every instant. Noticeably, inverting Eq. (11) can be performed numerically offline, rather than during the integration of the dynamic equations, drastically reducing the computational effort. For example, Fig. 7 shows φ_{im} as a function of φ_{iN}, for four different values of $\bar{\varphi}_i$, i.e., for four different shapes of the slider. This is obtained by directly computing Eq. (11) for discrete values of φ_{im} ranging from $-\pi/2 - \bar{\varphi}_i$ to $\pi/2 + \bar{\varphi}_i$. A linear interpolation of this function ensures a rapid and sufficiently accurate evaluation of the pressure distribution during simulation.

As the second step of the procedure, Eq. (1) is recalled to obtain the distribution of the infinitesimal friction forces dV_i on the ith interface, and the equivalence is then imposed between such distribution and the resultant force V_i (Fig. 4). By imposing the equivalence along x_{i0}, along z_{i0}, and around O_i, the following equations are, respectively, obtained:
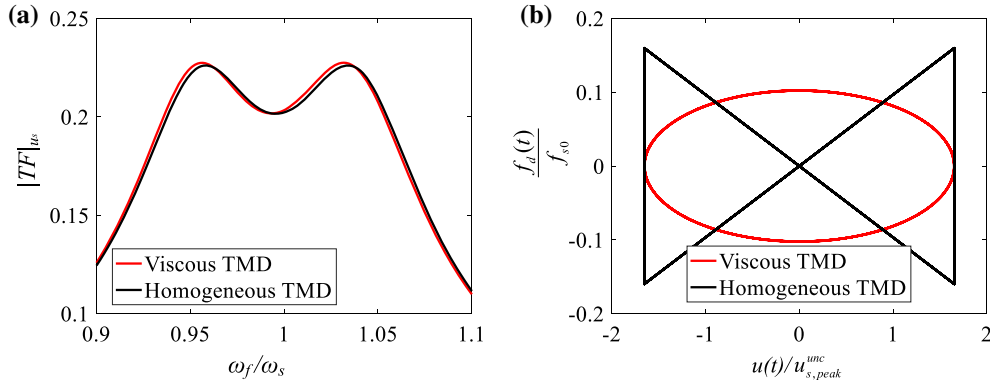
Fig. 8 Steady-state response of an SDOF structure under a harmonic force input, controlled with a linear viscous TMD or with a homogeneous friction TMD ($\zeta_s = 1\%$, $m_R = 1\%$): **a** TFs for the two optimal TMDs; **b** dissipative force–displacement loops for the two optimal TMDs (at $\omega_f = \omega_s$)

$$V_i \cos \varphi_{iV} = \operatorname{sgn} \dot{\theta} \int_{A_i} \cos \varphi_i \, dV_i, \tag{12}$$

$$V_i \sin \varphi_{iV} = \operatorname{sgn} \dot{\theta} \int_{A_i} \sin \varphi_i \, dV_i, \tag{13}$$

$$V_i \rho_{iV} = \operatorname{sgn} \dot{\theta} R_i \int_{A_i} \cos \psi_i \, dV_i. \tag{14}$$

Equations (12)–(14), with dV_i determined by Eqs. (1), (8), (9), and (11), represent the three constitutive contact equations, providing V_i, φ_{iV}, and ρ_{iV} as functions of N_i, φ_{iN}, θ, and $\dot{\theta}$, and directly usable in Eqs. (7.1)–(7.9). The evaluation of the integrals in their right-hand side must be performed numerically on each interface, accounting for a friction coefficient distribution that varies along the interface with time, as the slider moves across the two regions. Denoting with μ_i^a and μ_i^b the friction coefficients of the inner and outer regions (as shown in Figs. 1 and 2), and assuming that the inner region has the same dimensions of the slider, the distribution of the friction coefficient μ_i along the ith interface is expressed by the following step-wise function of $\bar{\varphi}_i$, θ, φ_i, and ψ_i:

$$\mu_i = \mu_i(\bar{\varphi}_i, \theta, \varphi_i, \psi_i) = \begin{cases} \mu_i^a, & \text{if } \cos \psi_i \cos(\varphi_i + \theta) \geq \cos \bar{\varphi}_i \\ \mu_i^b, & \text{if } \cos \psi_i \cos(\varphi_i + \theta) < \cos \bar{\varphi}_i \end{cases}. \tag{15}$$

With the friction coefficient distribution expressed by Eq. (15), a partially analytic solution of the integrals in Eqs. (12) to (14) becomes possible, which considerably reduces the computational effort. The procedure is reported in Appendix B and ultimately provides the values of $\int_{A_i} \cos \varphi_i \, dV_i$, $\int_{A_i} \sin \varphi_i \, dV_i$, and $\int_{A_i} \cos \psi_i \, dV_i$ as functions of the constant parameters R_i, $\bar{\varphi}_i$, μ_i^a, μ_i^b, and of the variables θ, σ_{im}, and φ_{im}.

On the other hand, the restrainer constitutive equation, providing F_i as a function of θ and $\dot{\theta}$, is defined as

$$F_i = [\operatorname{sgn} \theta \cdot k_{Fi}(|\theta| - \theta_{Fi}) + c_{Fi}\dot{\theta}]R_i \cdot \operatorname{step}(|\theta| - \theta_{Fi}). \tag{16}$$

Equation (16) represents a dissipative viscoelastic impact, occurring whenever $|\theta|$ exceeds an activation angle $\theta_{Fi} > 0$, and is governed by the stiffness k_{Fi} and the damping coefficient c_{Fi} of a Kelvin–Voigt spring–dashpot system placed along the sliding surface, i.e., at a distance R_i from O_i. Remarkably, if $\theta_{Fi} = 2\bar{\varphi}_i$, the restrainer is activated exactly when the slider entirely exits the inner region.

Equations (12)–(14) and Eq. (16) are the four constitutive equations at each sliding interface making the problem statically determined.

2.2.4 Integration of the equations of motion

The VFP-TMD response to an assigned acceleration input is obtained by solving Eq. (7.1), (7.2), (7.3), (7.4), (7.5), (7.6), (7.7), (7.8), and (7.9), supplemented with Eqs. (12)–(14), and (16). The integration is performed numerically using a MATLAB ODE solver, working in the state space according to the following incremental procedure, applied at every time step:

- The integrals in Eqs. (12)–(14) are computed according to Appendix B, based on the values of θ, σ_{im}, and φ_{im} obtained at the previous step.
- Equations (12)–(14) and (16) then provide $V_i \cos\varphi_{iV}$, $V_i \sin\varphi_{iV}$, $V_i \rho_{iV}$, and F_i as known functions of θ, and $\dot{\theta}$, making the TMD system completely described by Eqs. (7.1), (7.2), (7.3), (7.4), (7.5), (7.6), (7.7), (7.8), and (7.9).
- Denoting the state variables as $q_1 = \theta$ and $q_2 = \dot{\theta}$ and adding the further equation $\dot{q}_1 = q_2$, a system of 16 equations in 16 variables is obtained. The 16 equations are nonlinear w.r.t. the states, q_1 and q_2, but linear w.r.t. the state derivatives, $\dot{q}_1$ and $\dot{q}_2$, as well as w.r.t. the remaining following 14 variables: $N_i \cos\varphi_{iN}$ and $N_i \sin\varphi_{iN}$ (repeated 4 times, once for each interface), and N_3, V_3, M_3 (repeated twice, once for each bearing).
- Algebraically solving the linear system provides $\dot{q}_1$, $\dot{q}_2$ and the 14 variables as nonlinear functions of q_1 and q_2 and as linear functions of the acceleration input. The knowledge of $\dot{q}_1$ and $\dot{q}_2$ feeds the dynamic integration algorithm. The knowledge of the 14 variables provides N_i and φ_{iN} and ultimately σ_{im} and φ_{im} for the next step.

2.3 Reduced VFP-TMD models

The VFP-TMD model derived in Sect. 2.2 can represent any arrangement in Fig. 1, but gets simpler if some additional assumptions are made. Four possible reduced models are described below.

2.3.1 Reduced model $\mathtt{M}_1$: infinitely distant bearings

If the two bearings are infinitely distant from each other ($b \to \infty$), then they are subjected to the same values of N_3, V_3, M_3 and can be jointly modeled as a single bearing. The dynamic model reduces to Eq. (7.1)–(7.5) in the 5 variables θ, N_1, φ_{1N}, N_2, φ_{2N}, with V_3 and N_3 derived from Eq. (7.7) and (7.8) as follows:

$$V_3 = -[m_3 a_x + m_3 \rho_{1O2}(\ddot{\theta} \cos\theta - \dot{\theta}^2 \sin\theta)]/2, \tag{17.1}$$

$$N_3 = [m_3(g + a_z) + m_3 \rho_{1O2}(\ddot{\theta} \sin\theta + \dot{\theta}^2 \cos\theta)]/2. \tag{17.2}$$

M_3 is irrelevant for the integration and, if of interest, can be computed using Eq. (7.6).

2.3.2 Reduced model $\mathtt{M}_2$: infinitely distant symmetrical bearings with massless slider

If not only are the two bearings infinitely distant (as in model $\mathtt{M}_1$), but also their lower and upper surfaces are identical (symmetrical double VFP bearing) and the slider mass is negligible ($m_1 = 0$), then the two interfaces are symmetrically excited, i.e., $N_1 = N_2$, $\varphi_{1N} = \varphi_{2N}$, $V_1 = V_2$, $\varphi_{1V} = \varphi_{2V}$, $\rho_{1V} = \rho_{2V}$, $F_1 = F_2$. The dynamic model reduces to the following three equations in θ, N_1, and φ_{1N}:

$$m^*[L\ddot{\theta} + (g + a_z)\sin\theta + a_x \cos\theta] + N_1 \sin\varphi_{1N} + V_1 \cos\varphi_{1V} + F_1 \cos\bar{\varphi}_1 = 0, \tag{18.1}$$

$$m^*[(g + a_z)\cos\theta - a_x \sin\theta + L\dot{\theta}^2] - N_1 \cos\varphi_{1N} + V_1 \sin\varphi_{1V} + \mathrm{sgn}\,\theta \cdot F_1 \sin\bar{\varphi}_1 = 0, \tag{18.2}$$

$$J_1 \ddot{\theta} - N_1 L \sin\varphi_{1N} + V_1(\kappa\rho_{1V} - L\cos\varphi_{1V}) + F_1(\kappa R_1 - L\cos\bar{\varphi}_1) = 0 \tag{18.3}$$

where $m^* = m_2 + m_3/2$ is the amount of TMD mass pertaining to the individual bearing, L is the equivalent pendulum length, here coinciding with ρ_{1O2}, and κ is the multiplicative factor, here equal to 2.

2.3.3 Reduced model M_3: rocking P-TMD

If instead of a supported TMD a rocking TMD is considered (Fig. 1d), the upper TMD mass and the upper plate disappear. Equations (18.1), (18.2), and (18.3) are still valid, with $m^* = m_1$, $L = \rho_{1G1}$, and $\kappa = 1$.

2.3.4 Integration of the equations of motion for the reduced models M_2 and M_3

The integration procedure presented above for the general VFP-TMD model gets simpler for the reduced models M_2 and M_3, described by Eqs. (18.1), (18.2), and (18.3). Combining Eqs. (18.1) and (18.3) and rearranging Eq. (18.2) give

$$\ddot{\theta} = -\{Lm^*[(g + a_z)\sin\theta + a_x\cos\theta] + \kappa(V_1\rho_{1V} + F_1R_1)\}/J^*, \tag{19.1}$$

$$N_1\cos\varphi_{1N} = m^*[(g + a_z)\cos\theta - a_x\sin\theta + L\dot{\theta}^2] + V_1\sin\varphi_{1V} + \text{sgn}\,\theta \cdot F_1\sin\bar{\varphi}_1, \tag{19.2}$$

$$N_1\sin\varphi_{1N} = -\frac{J_1}{J^*}m^*[(g + a_z)\sin\theta + a_x\cos\theta] + V_1\left(\kappa\frac{m^*L\rho_{1V}}{J^*} - \cos\varphi_{1V}\right)$$
$$+ F_1\left(\kappa\frac{m^*LR_1}{J^*} - \cos\bar{\varphi}_1\right) \tag{19.3}$$

where $J^* = J_1 + m^*L^2$ is the rotational inertia around O_1 of the slider plus that of m^* supposed hinged in O_2. Introducing the state variables $q_1 = \theta$ and $q_2 = \dot{\theta}$, the following state space system is obtained:

$$\dot{q}_1 = q_2, \tag{20.1}$$
$$\dot{q}_2 = f_1(q_1, q_2, a_x, a_z), \tag{20.2}$$
$$N_1\cos\varphi_{1N} = f_2(q_1, q_2, a_x, a_z), \tag{20.3}$$
$$N_1\sin\varphi_{1N} = f_3(q_1, q_2, a_x, a_z) \tag{20.4}$$

where Eqs. (20.1) and (20.2) are the two first-order ODEs (respectively, linear and nonlinear) describing the evolution of the dynamic system, while Eqs. (20.3) and (20.4) are two algebraic equations updating N_1 and φ_{1N}.

2.4 The mechanical model of the VFP-TMD on an MDOF structure

Let us consider a linear multi-degree-of-freedom (MDOF) planar structure, modeled as an n_s-storey building having one lateral DOF per storey, with the VFP-TMD attached to the jth storey. Denoting by $\mathbf{u}_s$ the structural displacement vector, by $\mathbf{M}_s$, $\mathbf{C}_s$, and $\mathbf{K}_s$ the structural mass, damping, and stiffness matrices, by $\mathbf{f}_s$ the external force vector, and by $\ddot{u}_g$ and $\ddot{w}_g$ the horizontal and vertical ground acceleration components, the equation of motion of the ith storey is

$$m_{si}(\ddot{u}_g + \ddot{u}_{si}) + \mathbf{C}_{si}\dot{\mathbf{u}}_s + \mathbf{K}_{si}\mathbf{u}_s = f_{si} + \delta_{ij}\lambda_d, \, i = 1, 2, ..., n_s \tag{21}$$

where (i) the subscript i denotes the ith row of a vector/matrix, (ii) the topological operator δ_{ij} is 1 if $i = j$ and 0 otherwise, and (iii) λ_d is the horizontal component of the TMD reaction force, given by

$$\lambda_d = -\sum_k m_k[a_x + \ddot{x}_{1k}] = -\sum_k m_k[a_x + \rho_{1k}(\cos\theta\ddot{\theta} - \sin\theta\dot{\theta}^2)] \tag{22}$$

where the index k denotes the kth component of the TMD.

Equations (21) and (22), complemented with the equations of the VFP-TMD, are the equations of motion of the structure-TMD coupled system, with $a_x = \ddot{u}_g + \ddot{u}_{sj}$ and $a_z = \ddot{w}_g$ being the acceleration of the TMD support.

2.5 The simplified TMD model on a generalized SDOF structure

To better understand the VFP-TMD properties and to establish an optimal design method, some simplifications of the fully nonlinear models presented above are appropriate.

Regarding the structure, this is approximated as a generalized SDOF system.

Regarding the absorber, the following assumptions are made:

- The reduced model M_2 is adopted, expressed by Eqs. (19.1), (19.2) and (19.3) with $m^* = m_2 + m_3/2$, $L = \rho_{1O2}$ and $\kappa = 2$.

- The slider angular amplitude $\bar{\varphi}_1$ and the rotation θ are assumed very small, so only first-order terms are retained in their nonlinear expansions. Accordingly, any spherical region degenerates in its horizontal projection, so that $\rho_{1V} = R_1$.
- The normal contact force N_1 is supposed to be centered on A_1 (i.e., $\varphi_{1N} = \varphi_{1m} = 0$), as if the slider height were null ($h_1 = 0$).
- The vertical acceleration input is neglected ($a_z = 0$), as well as the slider inertia ($J_1 = 0$).

Under these assumptions, the pressure gets uniform on A_1 and equal to

$$\sigma_1 = \sigma_{1m} = \frac{N_1}{A_1} = \frac{m^* g}{A_1}, \tag{23}$$

the friction force consequently becomes

$$V_1 = \operatorname{sgn} \dot{\theta} \int_{A_1} dV_1 = \operatorname{sgn} \dot{\theta} \sigma_1 \int_{A_1} \mu_1 dA_1 = \operatorname{sgn} \dot{\theta} m^* g \mu_{\text{eff}1} \tag{24}$$

where

$$\mu_{\text{eff}1} = \frac{1}{A_1} \int_{A_1} \mu_1 dA_1 = \frac{1}{A_1} \left(\mu_1^a A_1^a + \mu_1^b A_1^b \right) = \mu_1^a + (\mu_1^b - \mu_1^a) \frac{A_1^b}{A_1}, \tag{25}$$

the VFP-TMD equation of motion becomes

$$L\ddot{\theta} + \operatorname{sgn} \dot{\theta} \eta g \mu_{\text{eff}1} + \eta F_1 / m^* + g\theta + a_x = 0, \tag{26}$$

and the overall TMD reaction force becomes:

$$\lambda_d = -m(a_x + L\ddot{\theta}) \tag{27}$$

where $\eta = 2R_1/L \geq 1$ and $m = 2m^*$ is the total TMD mass.

As a result of these simplifications, the coupled system is eventually described by

$$\ddot{u}_s + 2\zeta_s \omega_s \dot{u}_s + \omega_s^2 u_s = f_s/m_s - \ddot{u}_g - m_R(\ddot{u}_g + \ddot{u}_s + L\ddot{\theta}), \tag{28.1}$$

$$L\ddot{\theta} + \omega^2 L(\bar{f}_\mu + \bar{f}_F + \theta) = -(\ddot{u}_g + \ddot{u}_s) \tag{28.2}$$

where $\omega_s = \sqrt{k_s/m_s}$ is the structural circular frequency, $\zeta_s = c_s/(2\omega_s m_s)$ is the structural damping ratio, $m_R = m/m_s$ is the TMD mass ratio, $\omega = \sqrt{g/L}$ is the TMD circular frequency, $\bar{f}_F = \eta F_1/(m^* g)$ is the TMD normalized restrainer force, and

$$\bar{f}_\mu = \bar{f}_\mu(\theta, \dot{\theta}) = \eta V_1/(m^* g) = \operatorname{sgn} \dot{\theta} \eta \mu_{\text{eff}1} \tag{29}$$

is the TMD normalized equivalent friction force.

Equations (28.1) and (28.2) represents a linear system except for $\bar{f}_\mu$ and $\bar{f}_F$, intrinsically nonlinear. However, in the ideal case where $\mu_1^a = 0$, and for any $|\theta|$ not significantly larger than $2\bar{\varphi}_1$, $\mu_{\text{eff}1}$ can be approximated as a linear function of $|\theta|$, i.e., as $\mu_{\text{eff}1} = \tilde{\mu}_{\text{eff}1} |\theta|$. In fact, for $|\theta| \to 0$ the (tangential) linearized expression for $\mu_{\text{eff}1}$ can be derived as

$$\mu_{\text{eff}1} = \mu_{\text{eff}1}^+ = \frac{4}{\pi} \mu_1^b \frac{|\theta|}{2\bar{\varphi}_1} = \tilde{\mu}_{\text{eff}1}^+ |\theta| \tag{30}$$

while for $|\theta| = 2\bar{\varphi}_1$ the (secant) linearized expression for $\mu_{\text{eff}1}$ is

$$\mu_{\text{eff}1} = \mu_{\text{eff}1}^- = \mu_1^b \frac{|\theta|}{2\bar{\varphi}_1} = \tilde{\mu}_{\text{eff}1}^- |\theta| \tag{31}$$

where $\mu_{\text{eff}1}^- \leq \mu_{\text{eff}1}(\theta) \leq \mu_{\text{eff}1}^+$ for any $|\theta| \leq 2\bar{\varphi}_1$.

With this linearization, Eq. (29) becomes

$$\bar{f}_\mu = \bar{f}_\mu(\theta, \dot{\theta}) = \operatorname{sgn}(\dot{\theta}) \eta \tilde{\mu}_{\text{eff}1} |\theta| \tag{32}$$

where $\tilde{\mu}_{\text{eff}1}$ denotes either $\tilde{\mu}_{\text{eff}1}^-$ or $\tilde{\mu}_{\text{eff}1}^+$ depending on the expected range of θ, and the constant factor $\chi = \eta\tilde{\mu}_{\text{eff}1}$ is the friction ratio of the absorber, as defined in [22].

With all the previous assumptions, and as long as the collision with the restrainer is avoided, the VFP-TMD and hence the coupled system are nonlinear but homogeneous systems, and their response is proportional to the excitation amplitude. Because those assumptions and this result hold only to an approximate extent, Sect. 3 tests their validity by numerical simulations.

3 Design and simulation of the device

In this Section, a nearly optimal design procedure is first presented for VFP-TMDs, and then, the optimized absorber is simulated on SDOF and MDOF structures. For brevity, only the reduced model M_2 is addressed. The restrainer stiffness and damping parameters, k_{F1} and c_{F1}, excluded from optimization, are assigned to represent a relatively rigid inelastic impact. Recalling that in the M_2 model the lower and upper plates are connected by two identical restrainers placed in series, and denoting by $k_{Feq} = k_{F1}/2$ and $c_{Feq} = c_{F1}/2$ their equivalent coefficients, it is assumed that:

- $k_{F1} = 2k_{Feq} = 2\omega_{Feq}^2 m^*$, with $\omega_{Feq} = 10\omega$ [34];
- $c_{F1} = 2c_{Feq} = 4\zeta_{Feq}\omega_{Feq}m^*$, with $\zeta_{Feq} = -\dfrac{\ln e_{Feq}}{\sqrt{\pi^2 + \ln^2 e_{Feq}}}$, where e_{Feq} is the elastic restitution coefficient [35], here taken as 0.5.

3.1 Design methodology

Several TMD design approaches exist in the literature [36,37]. A nearly optimal criterion is here proposed for VFP-TMDs, based on the simplified model obtained in Sect. 2.5. Because that model is approximately homogeneous, the criterion is inspired by the optimal design method proposed for homogeneous P-TMDs in [22] and improved in [38]. Such method consists in a first-order H_∞ or H_2 optimum synthesis, minimizing the corresponding norm of an appropriate input–output transfer function (TF) of the structure-TMD system. A similar approach is adopted here, with due modifications accounting for VFP bearings features.

In detail, referring to the ideal case where $\mu_1^a = 0$, the design criterion comprises the following steps:

1. Identification of the structural damping ratio ζ_s and choice of the TMD mass ratio m_R.
2. Determination of the optimal values of the TMD frequency ratio, $\omega_R = \omega/\omega_s$, and the TMD friction ratio, $\chi = \eta\tilde{\mu}_{\text{eff}1}$, by minimizing the H_∞ or H_2 norm of a selected TF.
3. Derivation of the optimal equivalent pendulum length $L = \rho_{1O2} = g/\omega^2 = g/(\omega_R\omega_s)^2$.
4. Assumption of a value for the slider angular semi-width $\bar{\varphi}_1$.
5. Assumption of a value for the restrainer activation angle $\theta_{F1} \geq 2\bar{\varphi}_1$.
6. Assumption of a value for the height s_1 of the surface raised edge and derivation of (i) the sliding surface radius $R_1 = (L/2 + s_1)/\cos(\theta_{F1} + \bar{\varphi}_1)$, (ii) the ratio $\eta = 2R_1/L$; (iii) the slider semi-height $h_1 = R_1 - L/2 = R_1(1 - 1/\eta)$; and (iv) the slider aspect ratio $a_R = h_1/(R_1 \sin\bar{\varphi}_1) = (1 - 1/\eta)/\sin\bar{\varphi}_1$.
7. Determination of the optimal friction coefficient μ_1^b for the A_1^b region, computed as $\mu_1^b = \frac{\pi}{2}\tilde{\mu}_{\text{eff}1}\bar{\varphi}_1$ or as $\mu_1^b = 2\tilde{\mu}_{\text{eff}1}\bar{\varphi}_1$ depending if small or large displacements are expected; in these expressions, $\tilde{\mu}_{\text{eff}1}$ is computed as $\tilde{\mu}_{\text{eff}1} = \chi/\eta$ from the results of previous steps.
8. After simulations under the design loads, iterative improvement of $\bar{\varphi}_1$ and θ_{F1} in steps 4 and 5.

The above design criterion has two limitations: First, it is based on a simplified model that assumes small displacements and a flat surface. Second, it presumes a frictionless inner region ($\mu_1^a = 0$). These limitations are discussed in the sequel.

3.2 Simulations of the simplified VFP-TMD model on an SDOF structure

In this Section, the simplified TMD model presented in Sect. 2.5 is used to simulate the response of a VFP-TMD on an SDOF structure under a sinusoidal force input. That model, representing the nearly flat case, seems appropriate for a preliminary performance assessment, being simple enough to neglect the effects of geometrical nonlinearities and uneven contact pressure distributions, but also advanced enough to catch the

nonlinear dependence of the friction force and the restrainer force on θ, and the consequent control losses w.r.t. a perfectly homogeneous device. To highlight these losses, first a homogeneous TMD is considered in Sect. 3.2.1, and then, the actual VFP-TMD is analyzed in Sect. 3.2.2.

3.2.1 Perfectly homogeneous TMD

An SDOF structure having frequency ω_s and damping ratio $\zeta_s = 0.01$ is analyzed under a sinusoidal force having amplitude f_{s0}, circular frequency ω_f and duration sufficient to approximately induce a steady-state response. A TMD is considered, having mass ratio $m_R = 0.01$ and being either a perfectly linear viscous TMD or a perfectly homogeneous friction TMD. The viscous TMD is classically defined [7]. The friction TMD is defined by Eqs. (28.2) and (29), assuming $\bar{f}_F = 0$ (no restrainer) and $\mu_{\text{eff}1} = \tilde{\mu}_{\text{eff}1} |\theta|$, as per Eq. (30) or (31). For simplicity, admittedly, $s_1 = 0$, so that $\eta = 1$ and $\tilde{\mu}_{\text{eff}1} = \chi$. Both TMD types are designed to minimize the H_∞ norm of the *TF* from the force to the structural displacement [38]. Because both models are homogeneous (linearly or nonlinearly), the design solution is amplitude independent. The optimal parameters of the linear TMD are $\omega_R = 0.9886$ and $\zeta = 0.0625$ (ζ being the TMD viscous damping ratio); those of the homogeneous TMD are $\omega_R = 0.9971$ and $\tilde{\mu}_{\text{eff}1} = 0.1945$. Figure 8a compares the corresponding TFs, normalized to the uncontrolled TF peak $u_{s,peak}^{unc}$, which appear nearly identical. Figure 8b shows the corresponding steady-state dissipative force–displacement loops under a harmonic force having $\omega_f = \omega_s$. The two loops have different shapes but similar area, i.e., similar cyclic energy dissipation. The homogeneous friction TMD is concluded to be as effective as a linear TMD.

3.2.2 Actual VFP-TMD

In fact, even the VFP-TMD simplified model is homogeneous only in approximate terms and for limited values of θ. Its actual performance degrades for three reasons: (i) the dependence of $\mu_{\text{eff}1}$ on $|\theta|$ is nonlinear even if $\mu_1^a = 0$ and if $|\theta| \leq \theta_{F1}$; (ii) it may be that $\mu_1^a > 0$; (iii) it may be that $|\theta| > \theta_{F1}$ (restrainer activated). To examine this degradation, but also the advantages of the VFP-TMD over uniform-friction devices, four cases are considered:

- Case I: $\mu_1^a = 0$ & $\theta_{F1} \to \infty$
- Case II: $\mu_1^a = 0$ & $\theta_{F1} = 2\bar{\varphi}_1$
- Case III: $\mu_1^a = \mu_1^b$ & $\theta_{F1} \to \infty$
- Case IV: $\mu_1^a = \mu_1^b/10$ & $\theta_{F1} \to \infty$

Cases I and II represent the ideal condition of a frictionless inner region. In case I, the restrainer is inactive, while in case II it activates as the slider exits the inner region. Cases III and IV, both unrestrained, admit friction in the inner region. In particular, case III represents a uniform-friction P-TMD, while case IV represents a VFP-TMD in which μ_1^a is 10% of μ_1^b.

The structure is the same SDOF system assumed above ($\zeta_s = 0.01$), and the VFP-TMD is derived from the same optimal homogeneous TMD ($m_R = 0.01$, $\omega_R = 0.9971$, $\tilde{\mu}_{\text{eff}1} = \chi = 0.1945$), by further applying Eq. (30) to obtain μ_1^b from the assigned $\bar{\varphi}_1$. The system is still excited by a sinusoidal force of varying frequency and sufficient duration, but its amplitude f_{s0} is now varied, to highlight the amplitude dependence of the response. For the results to be independent from the assigned $\bar{\varphi}_1$, f_{s0} is normalized to $2mg\bar{\varphi}_1$, i.e., to the force which, statically applied to the TMD, would make the slider exit the inner region.

Results are reported in Figs. 9 and 10.

Figure 9 shows the TFs obtained in the four cases for 10 values of $f_{s0}/(2mg\bar{\varphi}_1)$ (from 0.01 to 10). Figure 9a–d shows the structural displacement, Fig. 9e–h the TMD displacement. The 8 subfigures are arranged in four columns, orderly referred to cases I to IV.

Figure 10 shows the peak of the same TFs as a function of $f_{s0}/(2mg\bar{\varphi}_1)$, for the four cases. Figure 10a shows the structural displacement and Fig. 10b the TMD displacement. The black dashed line in Fig. 10b represents the TMD displacement at which the TMD exits the inner region.

Figures 9 and 10 show that:

- Cases I and II substantially ensure the same performance of a homogeneous TMD as long as $f_{s0}/(2mg\bar{\varphi}_1) \leq 1.15$, i.e., as long as $|\theta| \leq 2\bar{\varphi}_1$. In this range, the nonlinear dependence of $\mu_{\text{eff}1}$ on $|\theta|$ does not practically affect effectiveness.
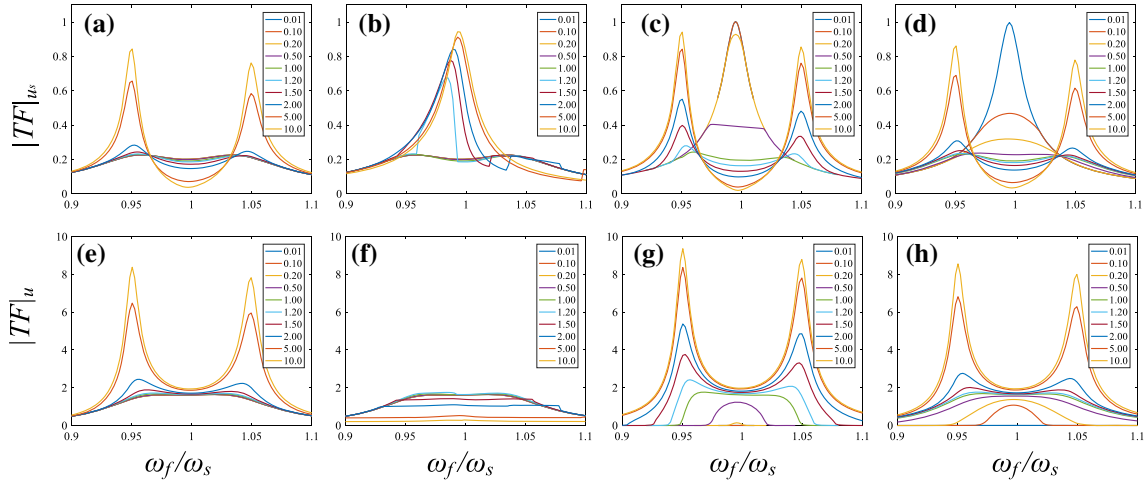
Fig. 9 Amplitude dependence of the input–output transfer functions (TFs) in the assumption of the simplified model. Top subfigures: force-to-structural displacement TFs. Bottom subfigures: force-to-TMD displacement TFs. **a** and **e**: Case I. **b** and **f**: Case II. **c** and **g**: Case III. **d** and **h**: Case IV. In each subfigure, TFs are drawn for 10 different values of the normalized force amplitude $f_{s0}/(2mg\bar{\varphi}_1)$, ranging from 0.01 to 10.0 (as per the legend)
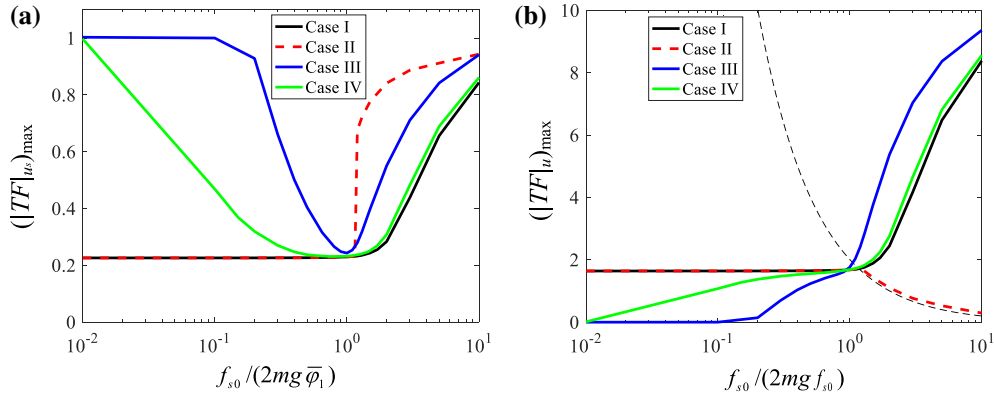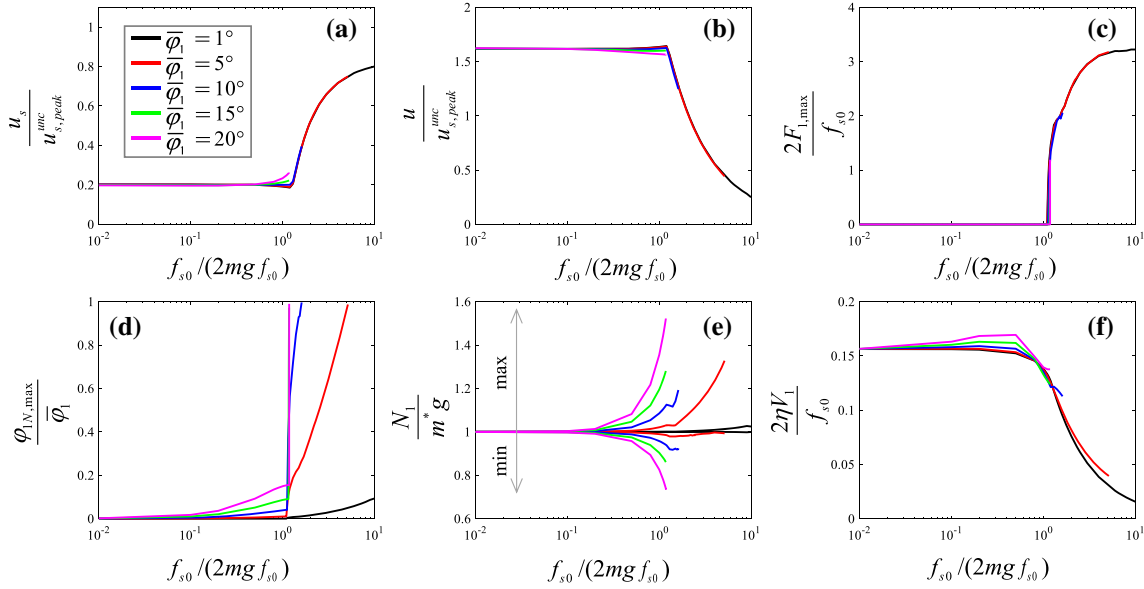

Fig. 10 Amplitude dependence of the peak value of the input–output TFs in the assumption of the simplified model. **a**: structural displacement. **b**: TMD displacement. Cases I to IV described in the legend. Black dashed line in subfigure b: $\theta = 2\bar{\varphi}_1$

- As $|\theta|$ exceeds $2\bar{\varphi}_1$, case I undergoes a gradual performance degradation, as $\mu_{\text{eff}1}$ can no longer increase beyond μ_1^b and the TMD equivalent damping ratio decreases. Case II, instead, undergoes a sudden degradation as the slider collides against the restrainer, worsening with increasing excitation. Softening the restrainer and/or increasing its activation angle will reduce and/or delay this degradation, but will also increase the bearing dimensions and the slider aspect ratio. This trade-off should be carefully considered in design.
- Case III shows the limitations of a uniform-friction TMD. Unrestrained as case I, case III achieves a similar performance only at a specific input amplitude (i.e., at $f_{s0}/(2\,mg\bar{\varphi}_1) \approx 1$), proving otherwise less effective, either because insufficiently damped (at larger amplitudes) or excessively damped (at smaller amplitudes). Under a certain input threshold, the friction force exceeds the inertial force on the TMD, which remains stuck to the structure.
- Case IV shows pros and cons of a plausible realization of VFP-TMD. It is nearly as effective as case I over a wide range of force amplitudes and still quite effective under amplitudes at which case III is totally useless. The complete inefficiency of the device occurs only at a very small input amplitude, 100 times smaller than that which activates the restrainer.

Table 1 Simulations of the rigorous VFP-TMD model on an SDOF structure—the 5 examined cases

Configuration	$\bar{\varphi}_1$	a_R	η	$\tilde{\mu}_{\text{eff}1}$	μ_1^b
	(°)	(–)	(–)	(–)	(%)
Case 1	1	0.079	1.0014	0.194	0.532
Case 2	5	0.391	1.0353	0.188	2.58
Case 3	10	0.772	1.1547	0.168	4.62
Case 4	15	1.132	1.4142	0.138	5.66
Case 5	20	1.462	2.0000	0.0972	5.33

Fig. 11 Amplitude dependence of the VFP-TMD response in the assumption of the rigorous model, for 5 values of $\bar{\varphi}_1$ (in the legend). Appropriately normalized, the following response quantities are reported: **a** structural displacement; **b** TMD displacement; **c** restrainer force; **d** offset angle; **e** normal contact force; **f** friction force

## 3.3 Simulations of the rigorous VFP-TMD model on an SDOF structure

If the rigorous VFP-TMD model is used instead of the simplified one, other interesting nonlinear phenomena are visible. The same SDOF structure examined before is reconsidered under a long-duration sinusoidal force having $\omega_f = \omega_s$. TMD parameters m_R, ω_R, and χ are also the same. Five VFP-TMDs are considered, with $\bar{\varphi}_1$ varying from 1° to 20° following Table 1. In all cases, $\theta_{F1} = 2\bar{\varphi}_1$, $\mu_1^a = 0$, and Eq. (30) holds, as in previous case II. Assuming $s_1 = 0$, the slider aspect ratio significantly increases with $\bar{\varphi}_1$, augmenting the slider's susceptibility to overturning under the couple of friction forces acting at its lower and upper surfaces. Also η increases with $\bar{\varphi}_1$, and $\tilde{\mu}_{\text{eff}1} = \chi_1/\eta$ and $\mu_1^b = \pi \tilde{\mu}_{\text{eff}1} \bar{\varphi}_1/2$ vary accordingly (Table 1).

In all cases, the normalized force amplitude $f_{s0}/(2mg\bar{\varphi}_1)$ is progressively increased (from 0.01 to 10) and the amplitude dependence of the response is observed.

Results are presented in Figs. 11 and 12.

In Fig. 11, $f_{s0}/(2mg\bar{\varphi}_1)$ is reported in the abscissae and various response quantities in the ordinates, namely the steady-state structural displacement u_s, normalized to $u_{s,\text{peak}}^{unc}$; the steady-state TMD displacement u, normalized to $u_{s,\text{peak}}^{unc}$; the maximum (over time) transient total restrainer force $2F_{1,\text{max}}$, normalized to f_{s0}; the maximum (over time) transient offset angle $\varphi_{1N,\text{max}}$, normalized to $\bar{\varphi}_1$; the steady-state minimum and maximum normal contact force N_1, normalized to m^*g; the steady-state total friction force $2V_1$, scaled times η and normalized to f_{s0}.

Figures 11a and 11b are similar to Figs. 10a and 10b. At a first glance, they show a similar performance of the 5 cases, with a nearly optimal effectiveness until restrainer activation, which approximately occurs at the same force amplitude for the 5 cases (Fig. 11c). After that, the structural displacement increases, and the TMD displacement decreases. A major difference, however, exists with respect to Fig. 10, because, except
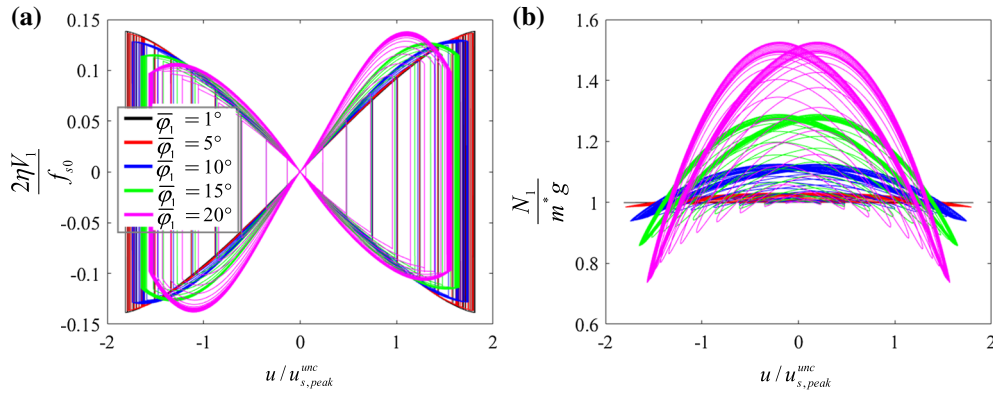
Fig. 12 Normalized friction force **(a)** and the normal contact force **(b)** versus the TMD displacement for 5 values of $\bar{\varphi}_1$ (in the legend), under the largest input amplitude with no restrainer activation

for $\bar{\varphi}_1 = 1°$, the curves are defined only until a certain threshold input amplitude, beyond which a steady-state response is no longer possible. At some instant during the transient response, in fact, $\varphi_{1N,\max}$ exceeds $\bar{\varphi}_1$ (Fig. 11d), i.e., N_1 exits the slider contour, and equilibrium is violated. Although a more comprehensive model, accounting for the slider detachment, might track the actual TMD behavior after that instant, the condition $\varphi_{1N,\max} = \bar{\varphi}_1$ reasonably defines a failure state. From Fig. 11c, such failure always follows the restrainer activation. The smaller $\bar{\varphi}_1$, the larger the margin from restrainer activation to failure. While for $\bar{\varphi}_1 = 1°$ this margin is conspicuous, for cases 4 and 5 failure immediately follows. Obviously, the susceptibility to overturning is related to the slider aspect ratio and therefore increasing with $\bar{\varphi}_1$ (Table 1). Another obvious effect of increasing $\bar{\varphi}_1$ is that geometric nonlinearities increase. This is evident in Fig. 11e, where the minimum and maximum normalized normal contact force (respectively, reached when $|u|$ is maximum and when u is zero) increasing diverge from 1 as $f_{s0}/(2mg\bar{\varphi}_1)$ increases and/or as $\bar{\varphi}_1$ increases. Less significant is, instead, the influence of $\bar{\varphi}_1$ on the friction force (Fig. 11f), nearly constant before the restrainer activation, and decreasing after it.

Finally, in Figs. 12a and 12b, the normalized friction force $2\eta V_1/f_{s0}$ and the normalized normal contact force $N_1/(m^*g)$ are plotted versus the normalized TMD displacement $u/u_{s,\text{peak}}^{unc}$. They are obtained, for each value of $\bar{\varphi}_1$, under the largest input force that does not activate the restrainer. The friction loops in Fig. 12a correspond to the triangular loops of a homogeneous model. For small $\bar{\varphi}_1$, the loops follow Eq. (25). For large $\bar{\varphi}_1$, the loops change with the instantaneous amplitude of the TMD strokes: for small amplitudes (in the first instants of the transient), the loops follow Eq. (25), while for large amplitudes (as the response becomes steady) they appear increasingly curved. As visible in Fig. 12b, this is because N_1 increasingly deviates from its static value as the TMD amplitude of motion increases. Because N_1 is maximum when $u = 0$ and minimum when $|u|$ is maximum, the ordinates of the friction loops increase with the motion amplitude for small values of $|u|$ and decrease with the motion amplitude for large values of $|u|$. Furthermore, the friction loops in Fig. 12a are asymmetric w.r.t. the horizontal axis because N_1 in Fig. 12b depends, for any value of u, on the direction of motion.

3.4 Simulation of the device on an MDOF structure

In this Section, the VFP-TMD is simulated on an MDOF high-rise building under wind excitation. The VFP-TMD design follows Sect. 3.1, and analyses adopt the fully nonlinear reduced model M$_2$. The VFP-TMD is compared with classical TMD types and observed under deviations of μ_1^a and μ_1^b from optimum.

3.4.1 The structure

The structure is the 42-storey high-rise building studied in [38], having a 168 m height and a 25×25 m^2 square section. The model is a planar 10-elements tapered cantilever beam, with a total mass of $22.69 \cdot 10^6$ kg. The first three modes have periods of 4.00 s, 1.23 s, and 0.52 s, and participating modal masses of 45.3%, 21.8%, and 11.1%. A 2% damping ratio ζ_s is assumed in every mode.

Table 2 Case study: maximum and rms responses to the along-wind component

Configuration	$u_{sN,\max}$	$u_{sN,rms}$	$a_{x,\max}$	$a_{x,rms}$	$u_{\max}$	u_{rms}	$\frac{V_{1,\max}}{m^*g}$	$\frac{F_{1,\max}}{m^*g}$	$\frac{\varphi_{1N}}{\bar{\varphi}_1}$
	(cm)	(cm)	(cm/s²)	(cm/s²)	(cm)	(cm)	(–)	(–)	(–)
Uncontrolled	15.8	5.0	47.4	13.3	–	–	–	–	–
Linear TMD	11.4	3.1	32.1	8.6	18.7	5.9	–	–	–
VFP-TMD – Case 1	11.0	3.1	32.3	9.8	17.5	5.9	0.018	0	0.01
VFP-TMD – Case 2	10.3	3.1	33.1	9.8	14.7	5.2	0.020	0	0.01
VFP-TMD – Case 3	11.0	3.4	41.4	10.5	9.9	3.5	0.027	0	0.01
VFP-TMD – Case 4	12.6	3.8	39.9	10.5	10.6	2.4	0.020	0	0.01

3.4.2 The wind load

The planar model is separately simulated under the along-wind or the across-wind components of a moderate-to-high wind flow, blowing for 60 min. Both components are applied to the structural nodes as deterministic wind load time histories, obtained as the realization of a stationary nonhomogeneous stochastic process, exactly defined as described in [38].

3.4.3 The VFP-TMD

The VFP-TMD is tuned to the structural fundamental mode ($\omega_s = 1.571$ rad/s), and its mass m is chosen as 1% the building mass ($m = 226900$ kg), corresponding to an 'effective' mass ratio $m_R = 6.45\%$. This assumption is the same as made in [38]. Because the structure and the wind loads are also the same, the results obtained here for the VFP-TMD can be compared with those obtained in [38] for other devices and for the uncontrolled building. Solving the H_∞ SDOF design problem for $\zeta_s = 2\%$ and $m_R = 6.45\%$ provides the VFP-TMD optimal dimensionless parameters, $\omega_R = 0.982$ and $\chi = 0.4524$, resulting in $\omega = \omega_R \cdot \omega_s = 1.542$ rad/s and $L = \rho_{1O2} = g/\omega^2 = 4122$ mm. Adopting $\theta_{F1} = 2\bar{\varphi}_1$, $\bar{\varphi}_1$ is tentatively assumed as 6°, resulting in $\theta_{F1} = 12°$. With $s_1 = 10$ mm, this implies $R_1 = 2177$ mm and $h_1 = 117$ mm, eventually producing a slider having height 233 mm and width 455 mm ($a_R = 0.512$) and a sliding surface having width 1346 mm. This also gives $\tilde{\mu}_{\mathrm{eff}1} = \chi/(2R_1/L) = 0.4282$. Once $\tilde{\mu}_{\mathrm{eff}}$ and $\bar{\varphi}_1$ are established, the optimal friction coefficient μ_1^b is to be determined, and an assumption is to be made about μ_1^a. To this regard, the following four cases are considered:

- Case 1: $\mu_1^b = \frac{\pi}{2}\tilde{\mu}_{\mathrm{eff}1}\bar{\varphi}_1 = 7.04\%$ & $\mu_1^a = 0$,
- Case 2: $\mu_1^b = 2\tilde{\mu}_{\mathrm{eff}1}\bar{\varphi}_1 = 8.97\%$ & $\mu_1^a = 0$,
- Case 3: $\mu_1^b = 4\tilde{\mu}_{\mathrm{eff}1}\bar{\varphi}_1 = 17.94\%$ & $\mu_1^a = 0$,
- Case 4: $\mu_1^b = \frac{10}{11}2\tilde{\mu}_{\mathrm{eff}1}\bar{\varphi}_1 = 8.15\%$ & $\mu_1^a = \frac{1}{10}\mu_1^b = 0.815\%$.

Cases 1 to 3 assume $\mu_1^a = 0$ (ideal case) and μ_1^b, respectively, given by Eq. (30), by Eq. (31), and by twice this latter value. Case 4 approximates case 2, assuming, more realistically, $\mu_1^a = \mu_1^b/10$ and $\mu_1^b = \frac{10}{11}2\tilde{\mu}_{\mathrm{eff}1}\bar{\varphi}_1$.

3.4.4 Results

Results of wind analyses are reported in Tables 2 and 3, respectively, for the along-wind and across-wind components; 6 configurations are compared in each Table. The first two configurations correspond to the uncontrolled structure and to the structure controlled via a linear TMD. The remaining four configurations correspond to the four VFP-TMD cases. Various response quantities are used to measure the absorber performance. Denoting by u_{sN} the top storey displacement, by a_x the top storey acceleration and by u the TMD horizontal stroke, those quantities include: maximum and rms structural displacement ($u_{sN,\max}$ and $u_{sN,rms}$), maximum and rms structural acceleration ($a_{x,\max}$ and $a_{x,rms}$), maximum and rms TMD stroke ($u_{\max}$, and u_{rms}), maximum normalized friction and restrainer forces ($V_{1,\max}/(m^*g)$ and $F_{1,\max}/(m^*g)$), and maximum normalized offset angle ($\varphi_{1N}/\bar{\varphi}_1$).

Furthermore, for the four VFP-TMD cases, the dissipative loops described by the normalized friction force $V_1/(m^*g)$ vs the TMD angular displacement θ are presented in Fig. 13a and 13b, respectively, for the along-wind and the across-wind components.

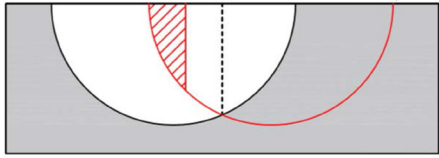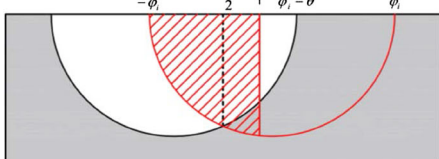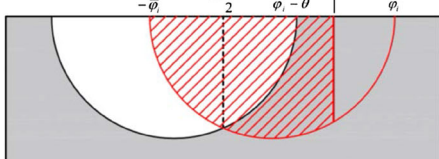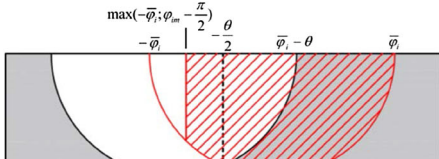**Table 3** Case study: maximum and rms responses to the across-wind component
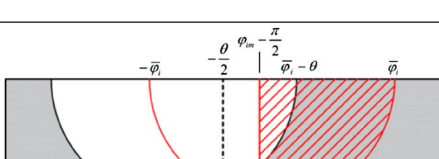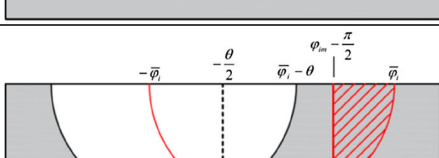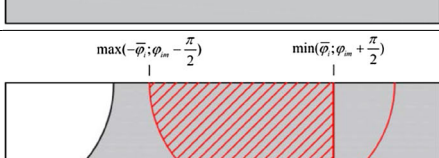
Configuration	$u_{sN,\max}$	$u_{sN,rms}$	$a_{x,\max}$	$a_{x,rms}$	$u_{\max}$	u_{rms}	$\dfrac{V_{1,\max}}{m^*g}$	$\dfrac{F_{1,\max}}{m^*g}$	$\dfrac{\varphi_{1N}}{\bar{\varphi}_1}$
	(cm)	(cm)	(cm/s^2)	(cm/s^2)	(cm)	(cm)	(–)	(–)	(–)
Uncontrolled	73.8	26.7	176.0	65.3	–	–	–	–	–
Linear TMD	35.5	11.8	85.3	28.2	99.2	33.0	–	–	–
VFP-TMD – Case 1	37.3	11.5	113.2	29.0	87.7	33.0	0.073	0.64	0.40
VFP-TMD – Case 2	34.6	12.0	96.2	30.7	78.1	29.1	0.086	0	0.05
VFP-TMD – Case 3	43.9	15.1	133.5	38.6	55.5	19.5	0.144	0	0.08
VFP-TMD – Case 4	34.9	12.4	95.6	30.9	81.2	27.6	0.079	0	0.04
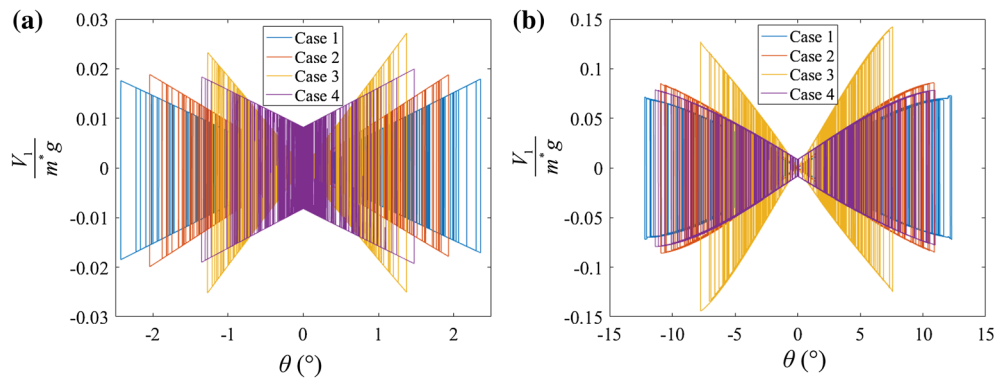
Fig. 13 Case study: friction force vs angular stroke dissipative loops for the four examined VFP-TMD cases, respectively, under: **a** the along-wind component; **b** the across-wind component

3.4.5 Discussion

Previous results can be commented as follows:

(i) For the uncontrolled structure, the response to the along-wind component is $4 \div 5$ times smaller than the response to the across-wind component, with the maximum displacement being, respectively, 16 cm (along wind) and 74 cm (across wind). These two load scenarios allow investigating the VFP-TMD performance under two significantly different input levels.

(ii) The linear TMD appears quite effective, particularly for the across-wind component (which induces larger dynamic amplifications). The max and rms structural response (in both displacement and acceleration) drops to 70% and 63% under the along-wind load and to 48% and 44% under the across-wind load. The maximum TMD displacement is 19 cm under the along-wind component and 99 cm under the across-wind component.

(iii) The VFP-TMD designed according to cases 1 and 2 achieves nearly the same performance as the linear TMD, under both wind components, with even a reduction in the TMD displacement. In case 1, such good performance occurs despite the activation of the restrainer under the across-wind load. In case 2, the larger friction ratio naturally reduces the TMD strokes and avoids bumping, slightly outperforming case 1. The similarity of cases 1 and 2 shows the VFP-TMD robustness to variations in its friction ratio.

(iv) The VFP-TMD designed according to case 3 proves less effective, with a significant increase in structural displacements and, even more, accelerations. This is the drawback of doubling the friction ratio. The advantage is the reduction in the TMD stroke, which decreases by 44% with respect to the linear TMD.

(v) The VFP-TMD described by case 4 resents the presence of friction in the inner region ($\mu_1^a > 0$), which diminishes control under low excitation levels. Compared to case 2, the TMD effectiveness diminishes against the less severe along-wind load, but keeps substantially unchanged against the across-wind load, also showing similar strokes. This proves that, even removing the zero friction assumption, still the VFP-TMD can achieve a satisfactory performance provided that μ_1^a is sufficiently smaller than μ_1^b.

(vi) The last three columns of Tables 2 and 3 indicate that only in one case the restrainer is activated and that relatively small friction forces are applied on the sliding surfaces. The normal contact force is generally

Case 1: $0 \le \theta \le 2\overline{\varphi}_i$ $-\overline{\varphi}_i - \frac{\pi}{2} \le \varphi_{im} \le -\frac{\theta}{2} - \frac{\pi}{2}$		$A_{ci}^a \begin{cases} -\overline{\varphi}_i \le \varphi_i \le \varphi_{im} + \frac{\pi}{2} \\ 0 \le \psi_i \le \psi_i^s \end{cases}$
Case 2: $0 \le \theta \le 2\overline{\varphi}_i$ $-\frac{\theta}{2} - \frac{\pi}{2} \le \varphi_{im} \le \overline{\varphi}_i - \theta - \frac{\pi}{2}$		$A_{ci}^a \begin{cases} -\overline{\varphi}_i \le \varphi_i \le -\frac{\theta}{2} \\ 0 \le \psi_i \le \psi_i^s \end{cases}$ $A_{ci}^a \begin{cases} -\frac{\theta}{2} \le \varphi_i \le \varphi_{im} + \frac{\pi}{2} \\ 0 \le \psi_i \le \psi_i^r \end{cases}$ $A_{ci}^b \begin{cases} -\frac{\theta}{2} \le \varphi_i \le \varphi_{im} + \frac{\pi}{2} \\ \psi_i^r \le \psi_i \le \psi_i^s \end{cases}$
Case 3: $0 \le \theta \le 2\overline{\varphi}_i$ $\overline{\varphi}_i - \theta - \frac{\pi}{2} \le \varphi_{im} \le 0$		$A_{ci}^a \begin{cases} -\overline{\varphi}_i \le \varphi_i \le -\frac{\theta}{2} \\ 0 \le \psi_i \le \psi_i^s \end{cases}$ $A_{ci}^a \begin{cases} -\frac{\theta}{2} \le \varphi_i \le \overline{\varphi}_i - \theta \\ 0 \le \psi_i \le \psi_i^r \end{cases}$ $A_{ci}^b \begin{cases} -\frac{\theta}{2} \le \varphi_i \le \overline{\varphi}_i - \theta \\ \psi_i^r \le \psi_i \le \psi_i^s \end{cases}$ $A_{ci}^b \begin{cases} \overline{\varphi}_i - \theta \le \varphi_i \le \min(\overline{\varphi}_i; \varphi_{im} + \frac{\pi}{2}) \\ 0 \le \psi_i \le \psi_i^s \end{cases}$
Case 4: $0 \le \theta \le 2\overline{\varphi}_i$ $0 \le \varphi_{im} \le -\frac{\theta}{2} + \frac{\pi}{2}$		$A_{ci}^a \begin{cases} \max(-\overline{\varphi}_i; \varphi_{im} - \frac{\pi}{2}) \le \varphi_i \le -\frac{\theta}{2} \\ 0 \le \psi_i \le \psi_i^s \end{cases}$ $A_{ci}^a \begin{cases} -\frac{\theta}{2} \le \varphi_i \le \overline{\varphi}_i - \theta \\ 0 \le \psi_i \le \psi_i^r \end{cases}$ $A_{ci}^b \begin{cases} -\frac{\theta}{2} \le \varphi_i \le \overline{\varphi}_i - \theta \\ \psi_i^r \le \psi_i \le \psi_i^s \end{cases}$ $A_{ci}^b \begin{cases} \overline{\varphi}_i - \theta \le \varphi_i \le \overline{\varphi}_i \\ 0 \le \psi_i \le \psi_i^s \end{cases}$
Case 5: $0 \le \theta \le 2\overline{\varphi}_i$ $-\frac{\theta}{2} + \frac{\pi}{2} \le \varphi_{im} \le \overline{\varphi}_i - \theta + \frac{\pi}{2}$		$A_{ci}^a \begin{cases} \varphi_{im} - \frac{\pi}{2} \le \varphi_i \le \overline{\varphi}_i - \theta \\ 0 \le \psi_i \le \psi_i^r \end{cases}$ $A_{ci}^b \begin{cases} \varphi_{im} - \frac{\pi}{2} \le \varphi_i \le \overline{\varphi}_i - \theta \\ \psi_i^r \le \psi_i \le \psi_i^s \end{cases}$ $A_{ci}^b \begin{cases} \overline{\varphi}_i - \theta \le \varphi_i \le \overline{\varphi}_i \\ 0 \le \psi_i \le \psi_i^s \end{cases}$
Case 6: $0 \le \theta \le 2\overline{\varphi}_i$ $\overline{\varphi}_i - \theta + \frac{\pi}{2} \le \varphi_{im} \le \overline{\varphi}_i + \frac{\pi}{2}$		$A_{ci}^b \begin{cases} \varphi_{im} - \frac{\pi}{2} \le \varphi_i \le \overline{\varphi}_i \\ 0 \le \psi_i \le \psi_i^s \end{cases}$
Case 7: $\theta > 2\overline{\varphi}_i$		$A_{ci}^b \begin{cases} \max(-\overline{\varphi}_i; \varphi_{im} - \frac{\pi}{2}) \le \varphi_i \le \\ \qquad \le \min(\overline{\varphi}_i; \varphi_{im} + \frac{\pi}{2}) \\ 0 \le \psi_i \le \psi_i^s \end{cases}$

Fig. 14 Assignment of the integration boundaries in Eqs. (A.11) and (A.12) in the 7 possible cases when $\theta \ge 0$. Left column: conditions on θ and φ_{im} for each case. Middle column: graphical representation of the 4 (or less) portions of the interface surface. Right column: identification the integration boundaries for A_{ci}^a and A_{ci}^b (ψ_i^s and ψ_i^r defined according to Eqs. (A.13) and (A.14))

quite centered on the sliding interface, except for case 1 under the across-wind load, when the maximum offset angle φ_{1N} equals $0.4\bar{\varphi}_1$, in which case $\varphi_{im} = 87.0°$ (partial decompression of the sliding interface).

(vii) Figures 13a and 13b compare the dissipative loops of the four VFP-TMD cases. Figure 13a shows a nearly linear increase of V_1 with θ, because of the small angular displacements occurring during along-wind load. In cases 1 to 3, the linear trend is also proportional (in fact homogeneous), and the loops pass through the origin with a slope dictated by μ_1^b. In case 4, the linear trend is no longer proportional, and the loops intersect the vertical axis at $V_{1,max}/(m^*g) = \pm\mu_1^a$. Figure 13b shows the curved loops typical of large angular displacements, with the vertical intersect of case 4 appearing less significant.

4 Conclusions

The VFP-TMD is presented in this paper, consisting of a mass supported on sliding pendulum bearings, in which each sliding surface is divided into two concentric regions: an inner circular region, having the lowest possible friction coefficient and the dimensions of the slider, and an outer annular region, with a friction coefficient set to an optimal value. To assess the VFP-TMD performance, its model is derived, a design methodology is established, and simulations are performed, comparing it with classical TMD types.

The main conclusions can be summarized as follows:

1. The proposed analytical model improves conventional models of sliding friction pendulums, and particularly existing models of VFP isolators, by considering (i) the spherical geometry of the problem, (ii) the effects of geometric nonlinearities, and (iii) the dependence of the friction force vector on the distributions of contact pressures along the sliding interface. From the rigorous general model, several simplified models are derived which can be useful in specific situations.
2. The proposed design methodology proves simple and effective. Fundamental design parameters are the slider angular width, $\bar{\varphi}_1$, and the restrainer activation angle, θ_{F1}, which governs: (i) bearing dimensions (i.e., cost); (ii) TMD displacement capacity (i.e., efficiency); (iii) slider aspect ratio (i.e., susceptibility to overturning). Other main design parameters are obviously the friction coefficients of the two regions, which should be kept as different as possible.
3. Numerical simulations have shown the influence of design parameters on VFP-TMD behavior in different design scenarios. In the ideal case of a frictionless inner region ($\mu_1^a = 0$), the VFP-TMD is substantially equivalent to a linear TMD, provided that no collision with the restrainer occurs; otherwise, a control loss is observed, whose mode and extent depend on $\bar{\varphi}_1$ (gradual loss with fully compressed interface at low $\bar{\varphi}_1$, sudden loss with incipient slider upheaval at large $\bar{\varphi}_1$). In the realistic case that $0 < \mu_1^a << \mu_1^b$, the effectiveness slightly decreases at small excitation levels but remains nearly optimal at large levels.
4. In all examined cases, the VFP-TMD achieves nearly the same effectiveness of viscous P-TMDs, while considerably outperforming conventional uniform-friction P-TMDs.

Appendix A—Evaluation of the B_i functions in Eqs. (9) and (10)

The functions B_1 and B_2 introduced in Eqs. (9) and (10) are defined, respectively, as

$$B_1(\bar{\varphi}_i, \varphi_{im}) = \frac{1}{R_i^2} \left[\cos\varphi_{im} \int_{A_{ci}} \cos^2\varphi_i \cos^2\psi_i dA_i + \sin\varphi_{im} \int_{A_{ci}} \sin\varphi_i \cos\varphi_i \cos^2\psi_i dA_i \right]$$

$$= \cos \varphi_{\mathrm{im}} \int\limits_{A_{ci}} \cos^2 \varphi_i \cos^2 \psi_i d\varphi_i d\psi_i + \sin \varphi_{\mathrm{im}} \int\limits_{A_{ci}} \sin \varphi_i \cos \varphi_i \cos^2 \psi_i d\varphi_i d\psi_i$$

$$= \cos \varphi_{\mathrm{im}} B_{11}(\bar{\varphi}_i, \varphi_{\mathrm{im}}) + \sin \varphi_{\mathrm{im}} B_{12}(\bar{\varphi}_i, \varphi_{\mathrm{im}}) \tag{A.1}$$

and as

$$lB_2(\bar{\varphi}_i, \varphi_{\mathrm{im}}) = \frac{1}{R_i^2} \left[\cos \varphi_{\mathrm{im}} \int\limits_{A_{ci}} \sin \varphi_i \cos \varphi_i \cos^2 \psi_i dA_i + \sin \varphi_{\mathrm{im}} \int\limits_{A_{ci}} \sin^2 \varphi_i \cos^2 \psi_i dA_i \right]$$

$$= \cos \varphi_{\mathrm{im}} \int\limits_{A_{ci}} \sin \varphi_i \cos \varphi_i \cos^2 \psi_i d\varphi_i d\psi_i + \sin \varphi_{\mathrm{im}} \int\limits_{A_{ci}} \sin^2 \varphi_i \cos^2 \psi_i d\varphi_i d\psi_i$$

$$= \cos \varphi_{\mathrm{im}} B_{12}(\bar{\varphi}_i, \varphi_{\mathrm{im}}) + \sin \varphi_{\mathrm{im}} B_{22}(\bar{\varphi}_i, \varphi_{\mathrm{im}}) \tag{A.2}$$

where B_{11}, B_{12} and B_{22} are given as follows:

$$B_{11}(\bar{\varphi}_i, \varphi_{\mathrm{im}}) = \int\limits_{A_{ci}} \cos^2 \varphi_i \cos^2 \psi_i d\varphi_i d\psi_i = \int\limits_{\max(-\bar{\varphi}_i; \varphi_{\mathrm{im}}-\pi/2)}^{\min(\bar{\varphi}_i; \varphi_{\mathrm{im}}+\pi/2)} \cos^2 \varphi_i \left(2 \int\limits_0^{\psi_i^s} \cos^2 \psi_i d\psi_i \right) d\varphi_i$$

$$= \int\limits_{\max(-\bar{\varphi}_i; \varphi_{\mathrm{im}}-\pi/2)}^{\min(\bar{\varphi}_i; \varphi_{\mathrm{im}}+\pi/2)} \cos^2 \varphi_i \left[\cos \psi_i \sin \psi_i + \psi_i \right]_0^{\psi_i^s} d\varphi_i$$

$$= \int\limits_{\max(-\bar{\varphi}_i; \varphi_{\mathrm{im}}-\pi/2)}^{\min(\bar{\varphi}_i; \varphi_{\mathrm{im}}+\pi/2)} \cos^2 \varphi_i (\cos \psi_i^s \sin \psi_i^s + \psi_i^s) d\varphi_i, \tag{A.3}$$

$$B_{12}(\bar{\varphi}_i, \varphi_{\mathrm{im}}) = \int\limits_{A_{ci}} \sin \varphi_i \cos \varphi_i \cos^2 \psi_i d\varphi_i d\psi_i$$

$$= \int\limits_{\max(-\bar{\varphi}_i; \varphi_{\mathrm{im}}-\pi/2)}^{\min(\bar{\varphi}_i; \varphi_{\mathrm{im}}+\pi/2)} \sin \varphi_i \cos \varphi_i (\cos \psi_i^s \sin \psi_i^s + \psi_i^s) d\varphi_i, \tag{A.4}$$

$$B_{22}(\bar{\varphi}_i, \varphi_{\mathrm{im}}) = \int\limits_{A_{ci}} \sin^2 \varphi_i \cos^2 \psi_i d\varphi_i d\psi_i = \int\limits_{\max(-\bar{\varphi}_i; \varphi_{\mathrm{im}}-\pi/2)}^{\min(\bar{\varphi}_i; \varphi_{\mathrm{im}}+\pi/2)} \sin^2 \varphi_i (\cos \psi_i^s \sin \psi_i^s + \psi_i^s) d\varphi_i. \tag{A.5}$$

In Eqs. (A.3) to (A.5), the integration boundaries are chosen to delimit the compressed interface A_{ci}. The relation $\psi_i^s = \arccos(\cos \bar{\varphi}_i / \cos \varphi_i)$ expresses the ψ_i coordinate of the contour of A_{ci} as a function of its φ_i coordinate and of the geometric parameter $\bar{\varphi}_i$.

Appendix B—Evaluation of the integrals in Eqs. (17.1), (17.2) to (19.1), (19.2), (19.3)

This Appendix presents a procedure for evaluating the integrals in Eqs. (12) to (14) as functions of the constant parameters R_i, $\bar{\varphi}_i$, μ_i^a, μ_i^b and of the variables θ, σ_{im}, and φ_{im}. The procedure is partly analytical and partly numerical. Using Eqs. (1) and (8), the three said integrals can be expressed as follows:

$$\int\limits_{A_i} \cos \varphi_i dV_i = \sigma_{\mathrm{im}} \int\limits_{A_{ic}} \mu_i \cos \varphi_i \cos \psi_i \cos(\varphi_i - \varphi_{\mathrm{im}}) dA_i = \sigma_{\mathrm{im}} R_i^2 [\cos \varphi_{\mathrm{im}} E_{11} + \sin \varphi_{\mathrm{im}} E_{12}], \tag{B.1}$$

$$\int\limits_{A_i} \sin \varphi_i dV_i = \sigma_{\mathrm{im}} \int\limits_{A_{ic}} \mu_i \sin \varphi_i \cos \psi_i \cos(\varphi_i - \varphi_{\mathrm{im}}) dA_i = \sigma_{\mathrm{im}} R_i^2 [\cos \varphi_{\mathrm{im}} E_{12} + \sin \varphi_{\mathrm{im}} E_{22}], \tag{B.2}$$

$$\int\limits_{A_i} \cos\psi_i \, dV_i = \sigma_{\mathrm{im}} \int\limits_{A_{ic}} \mu_i \cos^2\psi_i \cos(\varphi_i - \varphi_{\mathrm{im}}) dA_i = \sigma_{\mathrm{im}} R_i^2 \left[\cos\varphi_{\mathrm{im}} E_{31} + \sin\varphi_{\mathrm{im}} E_{32}\right] \tag{B.3}$$

where

$$E_{11} = E_{11}(\bar{\varphi}_i, \mu_i^a, \mu_i^b, \varphi_{\mathrm{im}}, \theta) = \int\limits_{A_{ic}} \mu_i \cos^2\varphi_i \cos\psi_i \, d\varphi_i \, d\psi_i, \tag{B.4}$$

$$E_{12} = E_{12}(\bar{\varphi}_i, \mu_i^a, \mu_i^b, \varphi_{\mathrm{im}}, \theta) = \int\limits_{A_{ic}} \mu_i \sin\varphi_i \cos\varphi_i \cos\psi_i \, d\varphi_i \, d\psi_i, \tag{B.5}$$

$$E_{22} = E_{22}(\bar{\varphi}_i, \mu_i^a, \mu_i^b, \varphi_{\mathrm{im}}, \theta) = \int\limits_{A_{ic}} \mu_i \sin^2\varphi_i \cos\psi_i \, d\varphi_i \, d\psi_i, \tag{B.6}$$

$$E_{31} = E_{31}(\bar{\varphi}_i, \mu_i^a, \mu_i^b, \varphi_{\mathrm{im}}, \theta) = \int\limits_{A_{ic}} \mu_i \cos\varphi_i \cos^2\psi_i \, d\varphi_i \, d\psi_i, \tag{B.7}$$

$$E_{32} = E_{32}(\bar{\varphi}_i, \mu_i^a, \mu_i^b, \varphi_{\mathrm{im}}, \theta) = \int\limits_{A_{ic}} \mu_i \sin\varphi_i \cos^2\psi_i \, d\varphi_i \, d\psi_i. \tag{B.8}$$

If μ_i were uniform on A_{ic}, the integrals in Eqs. (B.4) to (B.8) would be similar to those in Eqs. (A.3) to (A.5). Instead, μ_i varies with $\bar{\varphi}_i$, θ, φ_i, and ψ_i as a step-wise function, according to Eq. (15). Consequently, the integration can still be performed similarly as in Eqs. (A.3) to (A.5), once the integration boundaries are properly redefined.

To this purpose, Eqs. (B.4) to (B.6) can be jointly expressed as

$$E_{jk} = \mu_i^a \int\limits_{A_{ic}^a} f_{jk}(\varphi_i) \cos\psi_i \, d\varphi_i \, d\psi_i + \mu_i^b \int\limits_{A_{ic}^b} f_{jk}(\varphi_i) \cos\psi_i \, d\varphi_i \, d\psi_i \tag{B.9}$$

while Eqs. (B.7) and (B.8) as

$$E_{jk} = \mu_i^a \int\limits_{A_{ic}^a} f_{jk}(\varphi_i) \cos^2\psi_i \, d\varphi_i \, d\psi_i + \mu_i^b \int\limits_{A_{ic}^b} f_{jk}(\varphi_i) \cos^2\psi_i \, d\varphi_i \, d\psi_i \tag{B.10}$$

where $f_{jk}(\varphi_i)$ are the various trigonometric functions of φ_i appearing in Eqs. (B.4) to (B.8) and A_{ci}^a and A_{ci}^b are the portions of the compressed part of the ith interface, respectively, belonging to regions "a" and "b."

The first integral in Eq. (B.9) can be expressed as

$$\int\limits_{A_{ic}^a} f_{jk}(\varphi_i) \cos\psi_i \, d\varphi_i \, d\psi_i = \int\limits_{\varphi_i^{a-}}^{\varphi_i^{a+}} f_{jk}(\varphi_i) \left(2 \int\limits_{\psi_i^{a-}}^{\psi_i^{a+}} \cos\psi_i \, d\psi_i \right) d\varphi_i$$

$$= 2 \int\limits_{\varphi_i^{a-}}^{\varphi_i^{a+}} f_{jk}(\varphi_i)(\sin\psi_i^{a+} - \sin\psi_i^{a-}) d\varphi_i \tag{B.11}$$

where φ_i^{a-}, φ_i^{a+}, $\psi_i^{a-} = \psi_i^{a-}(\varphi_i)$ and $\psi_i^{a+} = \psi_i^{a+}(\varphi_i)$ denote the integration boundaries of the one half of A_{ci}^a, characterized by $\psi_i \geq 0$ (hence the factor "2" in the right-hand side term).

With identical notation, the first integral in Eq. (B.10) can be expressed as

$$\int\limits_{A_{ic}^a} f_{jk}(\varphi_i) \cos^2\psi_i \, d\varphi_i \, d\psi_i = \int\limits_{\varphi_i^{a-}}^{\varphi_i^{a+}} f_{jk}(\varphi_i) \left(2 \int\limits_{\psi_i^{a-}}^{\psi_i^{a+}} \cos^2\psi_i \, d\psi_i \right) d\varphi_i$$

$$= \int\limits_{\varphi_i^{a-}}^{\varphi_i^{a+}} f_{jk}(\varphi_i)(\cos \psi_i^{a+} \sin \psi_i^{a+} + \psi_i^{a+} - \cos \psi_i^{a-} \sin \psi_i^{a-} - \psi_i^{a-})d\varphi_i.$$

(B.12)

The second integrals in Eqs. (B.10) and (B.11) can be expressed similarly, with only the "b" superscript replacing the "a" superscript.

Once the integration boundaries are appropriately identified, the integrals in Eqs. (B.11) and (B.12) can be computed numerically, because their integrands are functions of the single variable φ_i. This determines first the functions E_{jk} in Eqs. (B.4) to (B.8) and ultimately the integrals in Eqs. (B.1) to (B.3).

Therefore, the crucial point is now to correctly identify the integration boundaries for both A_{ci}^a and A_{ci}^b.

To this purpose, it should be observed that in general the interface is delimited and subsequently parted (in four or less portions), by three or less characteristic lines. The four portions are regions "a" and "b," each further divided into a "compressed" portion and a "decompressed" portion. The three lines are, respectively, the contour of the slider given by

$$\psi_i = \psi_i^s = \arccos\left(\cos \bar{\varphi}_i / \cos \varphi_i\right),$$

(B.13)

the contour of the inner region given by

$$\psi_i = \psi_i^r = \arccos[\cos \bar{\varphi}_i / (\cos \varphi_i \cos \theta - \sin \varphi_i \sin \theta)],$$

(B.14)

and the neutral axis given by

$$\varphi_i = \varphi_{\text{im}} - \text{sgn}(\varphi_{\text{im}}) \cdot \pi/2.$$

(B.15)

Depending on how the three lines mutually intersect to generate the four or less portions of the interface, the integration boundaries take different values. Figure 14 shows the 7 possible cases corresponding to $\theta \geq 0$ (the cases corresponding to $\theta < 0$ are similar and omitted for brevity). The first 6 cases refer to $0 \leq \theta \leq 2\bar{\varphi}_i$ (corresponding to the slider intersecting the inner region), and are ordered for increasing values of φ_{im}. The 7th case refers to $\theta > 2\bar{\varphi}_i$ (corresponding to the slider being entirely comprised into the outer region). Each subfigure schematically represents the inner region "a" in white color, the outer region "b" in gray color, the slider contour and the neutral axis in red lines, the compressed interface in red hatching. For brevity, only half the space is represented, corresponding to $\psi_i \geq 0$, coherently with the integration boundaries defined in Eqs. (B.11) and (B.12). Beside each subfigure, the corresponding integration boundaries for A_{ci}^a and A_{ci}^b are reported, expressed in terms of φ_i and ψ_i.

With the integration boundaries of Fig. 14, all terms in Eq. (B.11) and (B.12) are known, so the respective integrals can be numerically evaluated by appropriately discretizing the φ_i axis, therefore providing the first terms of Eqs. (B.9) and (B.10), referring to A_{ci}^a. The second terms of Eqs. (B.9) and (B.10), referring to A_{ci}^b, are obtained in the same way. The three integrals in Eqs. (B.1) to (B.3) are finally obtained by applying Eqs. (B.1) to (B.8).

References

1. Marano, G.C., Greco, R., Palombella, G.: Stochastic optimum design of linear tuned mass dampers for seismic protection of high towers. Struct. Eng. Mech. **29**(6), 603–622 (2008)
2. Huang, M.F., Tse, K.T., Chan, C.M., Lou, W.J.: Integrated structural optimization and vibration control for improving wind-induced dynamic performance of tall buildings. Int. J. Struct. Stab. Dyn. **11**(6), 1139–1161 (2011)
3. Ruiz, R., Taflanidis, A.A., Lopez-Garcia, D., Vetter, C.R.: Life-cycle based design of mass dampers for the Chilean region and its application for the evaluation of the effectiveness of tuned liquid dampers with floating roof. Bull. Earthq. Eng. **14**, 943–970 (2016)
4. Greco, R., Marano, G.C., Fiore, A.: Performance-cost optimization of tuned mass damper under low-moderate seismic actions. Struct. Des. Tall Spec. Build. **25**(18), 1103–1122 (2016)
5. Elias, S., Matsagar, V.: Research developments in vibration control of structures using passive tuned mass dampers. Annu. Rev. Control **44**, 129–156 (2017)
6. Matta, E.: Lifecycle cost optimization of tuned mass dampers for the seismic improvement of inelastic structures. Earthq. Eng. Struct. Dyn. **47**, 714–737 (2017)
7. Warburton, G.B.: Optimum absorber parameters for various combinations of response and excitation parameters. Earthq. Eng. Struct. Dyn. **10**(3), 381–401 (1982)

8. Almazan, J.L., De la Llera, J.C., Inaudi, J.A., Lopez-Garcia, D., Izquierdo, L.E.A.: Bidirectional and homogeneous tuned mass damper: a new device for passive control of vibrations. Eng. Struct. **29**(7), 1548–1560 (2007)
9. Legeza, V.P.: Dynamics of vibroprotective systems with roller dampers of low-frequency vibrations. Strength Mat. **36**(2), 185–194 (2004)
10. Matta, E., De Stefano, A.: Seismic performance of pendulum and translational roof-garden TMDs. Mech. Syst. Signal Process. **23**, 908–921 (2009)
11. Náprstek, J., Fischer, C., Pirner, M., Fischer, O.: Non-linear model of a ball vibration absorber. Comput. Methods Appl. Sci. **30**, 381–396 (2013)
12. Bransch, M.: Unbalanced oil filled sphere as rolling pendulum on a flat surface to damp horizontal structural vibrations. J. Sound Vib. **368**, 22–35 (2016)
13. Wang, J., Wierschem, N.E., Spencer Jr., B.F., Lu, X.: Numerical and experimental study of the performance of a single-sided vibro-impact track nonlinear energy sink. Earthq. Eng. Struct. Dyn. **4**(4), 635–652 (2016)
14. Matta, E., De Stefano, A., Spencer Jr., B.F.: A new passive rolling-pendulum vibration absorber using a non-axial-symmetrical guide to achieve bidirectional tuning. Earthq. Eng. Struct. Dyn. **38**(15), 1729–1750 (2009)
15. Pirner, M.: Actual behaviour of a ball vibration absorber. J. Wind Eng. Ind. Aerodyn. **90**, 987–1005 (2002)
16. Chen, J., Georgakis, C.T.: Tuned rolling-ball dampers for vibration control in wind turbines. J. Sound Vib. **332**(21), 5271–5282 (2013)
17. Zhang, Z.L., Chen, J.B., Li, J.: Theoretical study and experimental verification of vibration control of offshore wind turbines by a ball vibration absorber. Struct. Infrastruct. Eng. **10**(8), 1087–1100 (2014)
18. Li, S., Fu, L., Kong, F.: Seismic response reduction of structures equipped with a voided biaxial slab-based tuned rolling mass damper. Shock Vib. **760394**, 1–15 (2015)
19. Fiore, A., Marano, G.C., Natale, M.N.: Theoretical prediction of the dynamic behavior of rolling-ball rubber-layer isolation systems. Struct. Control Health. Monit. **23**, 1150–1167 (2016)
20. Ricciardelli, F., Vickery, B.J.: Tuned vibration absorbers with dry friction damping. Earthq. Eng. Struct. Dyn. **28**(7), 707–723 (1999)
21. Inaudi, J., Kelly, J.: Mass damper using friction-dissipating devices. J. Eng. Mech. **121**(1), 142–149 (1995)
22. Matta, E.: A novel bidirectional pendulum tuned mass damper using variable homogeneous friction to achieve amplitude-independent control. Earthq. Eng. Struct. Dyn. **48**, 653–677 (2019)
23. Matta, E.: Ball vibration absorbers with radially-increasing rolling friction. Mech. Syst. Signal Process. **132**, 353–379 (2019)
24. Panchal, V.R., Jangid, R.S.: Seismic response of structures with variable friction pendulum system. J. Earthq. Eng. **13**, 193–216 (2009)
25. Kong, D., Fan, F., Zhi, X.: Seismic Performance of Single-Layer Lattice Shells with VF-FPB. Int. J. Steel Struct. **14**(4), 901–911 (2014)
26. Calvi, P.M., Moratti, M., Calvi, G.M.: Seismic isolation devices based on sliding between surfaces with variable friction coefficient. Earthq. Spectra **32**(4), 2291–2315 (2016)
27. Calvi, P.M., Ruggiero, D.M.: Numerical modelling of variable friction sliding base isolators. Bull. Earthq. Eng. **14**(2), 549–568 (2016)
28. Timsina, S., Calvi, P.M.: Variable Friction Base Isolation Systems: Seismic Performance and Preliminary Design. J. Earthq. Eng. (2018). https://doi.org/10.1080/13632469.2018.1504837
29. Weber, F., Distl, J., Meier, L., Braun, C.: Curved surface sliders with friction damping, linear viscous damping, bow tie friction damping, and semiactively controlled properties. Struct. Control Health. Monit. **25**, e2257 (2018)
30. Zayas, V., Low, S., Mahin, S.: The FPS earthquake resistant system, Experimental report UC Berkeley (Report No. UCB/EERC-87/01) (1987)
31. Malekzadeh, M., Taghikhany, T.: Adaptive behavior of double concave friction pendulum bearing and its advantages over friction pendulum systems. Sci. Iran. **17**(2), 81–88 (2010)
32. Fenz, D.M., Constantinou, M.C.: Spherical sliding isolation bearings with adaptive behavior: experimental verification. Earthq. Eng. Struct. Dyn. **37**(2), 185–205 (2008)
33. Tsai, C.S., Lin, Y.C., Su, H.C.: Characterization and modeling of multiple friction pendulum isolation system with numerous sliding interfaces. Earthq. Eng. Struct. Dyn. **39**, 1463–91 (2010)
34. Lu, Z., Wang, Z., Masri, S.F., Lu, X.: Particle impact dampers: past, present, and future. Struct. Control Health Monit. **25**(1), e2058 (2017)
35. Shäfer, J., Dippel, S., Wolf, D.: Force schemes in simulations of granular materials. Aust. J. Physiother. **6**(1), 5–20 (1996)
36. Marano, G.C., Greco, R.: Robust optimum design of tuned mass dampers for high-rise buildings under moderate earthquakes. Struct. Design Tall Special Build. **18**(8), 823–838 (2009)
37. Greco, R., Marano, G.C.: Optimum design of Tuned Mass Dampers by displacement and energy perspectives. Soil Dyn. Earthq. Eng. **49**, 243–253 (2013)
38. Matta, E.: Modeling and design of bidirectional pendulum tuned mass dampers using axial or tangential homogeneous friction damping. Mech. Syst. Signal Process. **116**, 392–414 (2019)